Physical topology of three-dimensional unsteady flows with spheroidal invariant surfaces

P. S. Contreras,[1,2] M. F. M. Speetjens,[1] and H. J. H. Clercx[2]
[1]*Section Energy Technology and Fluid Dynamics and J. M. Burgers Center for Fluid Dynamics, Department of Mechanical Engineering, Eindhoven University of Technology, Eindhoven, The Netherlands*
[2]*Section Fluids and Flows and J. M. Burgers Center for Fluid Dynamics, Department of Applied Physics, Eindhoven University of Technology, Eindhoven, The Netherlands*

(Received 23 April 2020; accepted 8 May 2020; published 27 May 2020)

Scope is the response of Lagrangian flow topologies of three-dimensional time-periodic flows consisting of spheroidal invariant surfaces to perturbation. Such invariant surfaces generically accommodate nonintegrable Hamiltonian dynamics and, in consequence, intrasurface topologies composed of islands and chaotic seas. Computational studies predict a response to arbitrary perturbation that is dramatically different from the classical case of toroidal invariant surfaces: said islands and chaotic seas evolve into tubes and shells, respectively, that merge into "tube-and-shell" structures consisting of two shells connected via (a) tube(s) by a mechanism termed "resonance-induced merger" (RIM). This paper provides conclusive experimental proof of RIM and advances the corresponding structures as the physical topology of realistic flows with spheroidal invariant surfaces; the underlying unperturbed state is a singular limit that exists only for ideal conditions and cannot be achieved in a physical experiment. This paper furthermore expands existing theory on certain instances of RIM to a comprehensive theory (supported by experiments) that explains *all* observed instances of this phenomenon. This theory reveals that RIM ensues from perturbed periodic lines via three possible scenarios: truncation of tubes by (i) manifolds of isolated periodic points emerging near elliptic lines or by either (ii) local or (iii) global segmentation of periodic lines into elliptic and hyperbolic parts. The RIM scenario for local segmentation includes a perturbation-induced change from elliptic to hyperbolic dynamics near degenerate points on entirely elliptic lines (denoted "virtual local segmentation"). This theory furthermore demonstrates that RIM indeed accomplishes tube-shell merger by exposing the existence of invariant surfaces that smoothly extend from the tubes into the chaotic shells. These phenomena set the response to perturbation—and physical topology—of flows with spheroidal invariant surfaces fundamentally apart from flows with toroidal invariant surfaces. Its entirely kinematic nature and reliance solely on continuity and solenoidality of the velocity field render the comprehensive theory and its findings universal and generically applicable for (arbitrary perturbation of) basically any incompressible flow—in fact any smooth solenoidal vector field—accommodating spheroidal invariant surfaces.

DOI: 10.1103/PhysRevE.101.053109

I. INTRODUCTION

The paper concerns the response of Lagrangian flow topologies of three-dimensional (3D) unsteady flows consisting of nontoroidal invariant surfaces to perturbation. The response scenarios for the classical case of toroidal invariant surfaces are well known: resonant and nonresonant tori disintegrate and survive, respectively, perturbation according to (3D counterparts of) the Poincaré-Birkhoff and Kolmogorov-Arnold-Moser (KAM) theorems [1–4]. Most tori generically survive weak perturbation and thus the unperturbed flow topology is largely retained. Surviving tori may develop defects due to local resonances (as opposed to global resonances causing tori breakdown as per the Poincaré-Birkhoff theorem) that, if occurring, result in gradual global dispersion of tracers through repeated "switching" between tori and crossing of separatrices [4–8].

Key to the response scenarios for toroidal invariant surfaces is intrasurface Lagrangian motion that generically consists of helical trajectories centered on the toroidal axis; both the Poincaré-Birkhoff and KAM theorems explicitly rely on this [1]. However, the dynamics inside nontoroidal invariant surfaces may be fundamentally different and thus invalidate said theorems and corresponding scenarios. A case of great practical relevance exists in spheroidal invariant surfaces encountered in 3D lid-driven cavity flows (serving as physical models for, e.g., batch mixers and bio-reactors yet also for flow in microdroplets or lung alveoli), tumblers for granular media, or (kinematic models for) 3D microfluidic flows induced by magnetic beads [9]. This furthermore includes quasi-two-dimensional (2D) geophysical flows, that is, large-scale oceanographic and atmospheric flows with an orientation parallel to the spherical surface of the Earth [10]; the Lagrangian motion in such flows is in the corresponding 2D limit topologically similar to that restricted to (subregions of) spheroidal invariant surfaces.

Spheroidal invariant surfaces in 3D unsteady flows generically accommodate nonintegrable Hamiltonian dynamics and, in consequence, intrasurface flow topologies composed (contrary to helical trajectories in tori) of islands and chaotic seas [11]. Computational studies predict a response to arbitrary perturbation that is dramatically different from tori: said

islands and chaotic seas evolve into tubes and shells, respectively, that merge into intricate "tube-and-shell" structures consisting of two shells connected via (a) tube(s). Such tube-shell merger was first observed in 3D time-periodic flows inside a lid-driven cylindrical cavity in [12–14]. The follow-up study in [15] on an external microflow driven by rotating magnetic beads revealed essentially the same tube-and-shell structures upon perturbation of the spheroidal invariant surfaces of the corresponding unperturbed limit. Moreover, the dynamics in the 3D time-periodic granular flow in a spherical tumbler investigated in [16] also exhibits the characteristics for perturbation-induced tube-shell merger, i.e., spheroidal invariant surfaces with nonintegrable Hamiltonian dynamics in the unperturbed state, yet without explicit exploration of this phenomenon. The findings particularly in [12–15] strongly suggest that the tube-and-shell structures constitute the physical topology of 3D unsteady flows with spheroidal invariant surfaces and the underlying unperturbed state is a singular limit. Similar Hamiltonian dynamics in fact occur in nontoroidal invariant surfaces of greater topological complexity [17] as well as in quasi-2D representations of Lagrangian transport in geophysical flows [18,19]. Hence, though beyond the present scope, the behavior associated with (perturbed) spheroidal invariant surfaces investigated below likely generalizes to a broader class of systems involving restriction of Lagrangian motion to (subregions of) nontoroidal invariant surfaces.

The above findings are to date only indirectly supported by experimental evidence [20]. Moreover, full explanation of the underlying mechanisms exists only for some instances of RIM; other manifestations of this phenomenon are beyond current theories. The principal goals of this paper therefore are (i) conclusive experimental validation of RIM (Sec. III) and (ii) development of a rigorous and comprehensive theory that explains *all* observed instances of RIM and demonstrates that this phenomenon indeed involves merger *of* (instead of random switching *between*) Lagrangian entities (Secs. IV–VI).

II. Physical VERSUS THEORETICAL TOPOLOGY

A. Configuration and unperturbed dynamics

The system considered by [20] is adopted as representative case for investigation of the dynamics of flows with spheroidal invariant surfaces and corresponds with the configuration of the above-mentioned computational studies that first exposed RIM [12–14]. It consists of a solenoidal time-periodic flow $\boldsymbol{u}(\boldsymbol{\xi},t)=\boldsymbol{u}(\boldsymbol{\xi},t+T)$ in a cylinder (radius R and height $H=2R$), with T the period time and $\boldsymbol{\xi}=(x_1,x_2,x_3)$ the Cartesian reference frame, driven by repetition of the sequence of piecewise steady translations of the bottom wall at velocity U and angles $\theta_k=2k\pi/3$ ($k\in\{0,1,2\}$) with the x axis and of duration $T/3$ (Fig. 1). The Lagrangian motion of passive tracers released in this flow at positions $\boldsymbol{\xi}(0)=\boldsymbol{\xi}_0$ is governed by the kinematic equation

$$\frac{d\boldsymbol{\xi}}{dt}=\boldsymbol{u}(\boldsymbol{\xi},t), \tag{1}$$

which admits formal solution by the mapping

$$\boldsymbol{\xi}_{n+1}=\boldsymbol{\Phi}(\boldsymbol{\xi}_n),\quad \boldsymbol{\xi}_n=\boldsymbol{\xi}(nT), \tag{2}$$

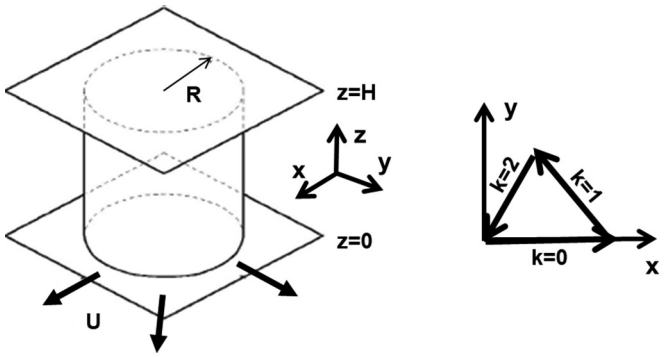

FIG. 1. Representative flow configuration: time-periodic flow inside a cylinder of radius R and height $H=2R$ driven by piecewise steady translations at velocity U of the bottom wall (left) under angle $\theta_k=2k\pi/3$ ($k\in\{0,1,2\}$) with the x axis (right).

with $n\geqslant 0$ the period. The sequence of consecutive tracer positions governed by (2), i.e.,

$$\mathcal{P}(\boldsymbol{\xi}_0)=\{\boldsymbol{\xi}_0,\boldsymbol{\xi}_1,\dots\}, \tag{3}$$

defines the stroboscopic map (or "Poincaré section") of a tracer starting at $\boldsymbol{\xi}_0$ and visualizes the Lagrangian transport. This stroboscopic map is synchronized with the start of the first wall ($\theta_1=0$) at time levels $t=nT$ ($n\geqslant 0$) in the periodic forcing sequence by the bottom wall. The system is parametrized by the nondimensional wall displacement $D=UT/3R$ (= 4 hereafter) and the Reynolds number $\mathrm{Re}=UR/\nu$, with ν the kinematic viscosity.

Lagrangian motion is in the Stokes limit $\mathrm{Re}=0$ confined to spheroidal invariant surfaces as demonstrated in Fig. 2(a) (left) by simulation of a stroboscopic map (black tracers) in a typical spheroid (cyan) using an analytical flow field following [20]. The corresponding projection in the rz plane [Fig. 2(a), right] clearly reveals this confinement. [Tracer positions in Fig. 2(a) (left) on the bottom side of the spheroid are visible only through its transparent surface and thus appear somewhat dim.] Transformation to a curvilinear reference frame $\boldsymbol{\zeta}=(\zeta_1,\zeta_2,\zeta_3)$, with Jacobian $J=|\partial\boldsymbol{\xi}/\partial\boldsymbol{\zeta}|$, such that coordinates (ζ_1,ζ_2) and ζ_3 are locally tangent and normal, respectively, to the spheroids translates the kinematic equation (1) into the Hamiltonian form

$$\frac{d\zeta_1}{dt}=\frac{1}{J}\frac{\partial\psi}{\partial\zeta_2},\quad \frac{d\zeta_2}{dt}=-\frac{1}{J}\frac{\partial\psi}{\partial\zeta_1}, \tag{4}$$

with $\psi(\boldsymbol{\zeta},t)$ the corresponding Hamiltonian. This implies intrasurface flow topologies characteristic of 2D nonautonomous Hamiltonian systems: islands surrounded by chaotic seas. The tracer in Fig. 2(a) occupies such a chaotic sea and outlines two intrasurface islands on opposite sides of the invariant surface (indicated by black arrows).

B. Impact of perturbations

The above Hamiltonian topology is the theoretical state yet constitutes a singular limit that changes dramatically under arbitrary perturbation. Introduce to this end a perturbation of the flow forcing of the Stokes limit $\mathrm{Re}=0$ by an additional translation of the top wall at an angle θ' relative to the stepwise translation direction θ_k and relative magnitude ϵU, with $\epsilon\ll$

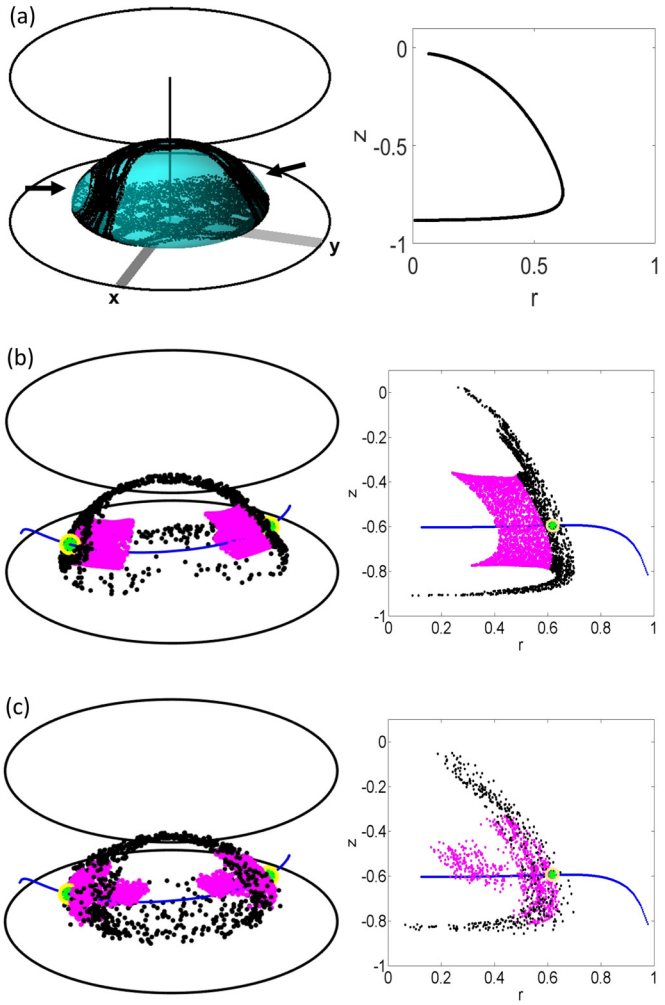

FIG. 2. Physical vs theoretical topology in flows with spheroidal invariant surfaces demonstrated by the stroboscopic map of a single tracer (left, 3D from identical viewpoints; right, rz projection) in time-periodic cylinder flow driven by stepwise translations of the bottom wall at angles $\theta_k = 2k\pi/3$ ($k \in \{0, 1, 2\}$) with the x axis. (a) Simulated theoretical topology (unperturbed limit Re = 0) of tracers (black) restricted to the chaotic sea in invariant surfaces (cyan/gray) and outlining intrasurface islands (black arrows). (b) Simulated physical topology of tube (magenta/gray) and shell (black) structures due to explicit perturbation by the top wall (Re = 0). (c) Experimental topology originating from natural disturbances. Blue, curve periodic line; green star/yellow circle, degenerate points.

1, following [20]. Figure 2(b) gives the stroboscopic map $\mathcal{P}(\boldsymbol{\xi}_0)$ for the same initial position $\boldsymbol{\xi}_0$ as in Fig. 2(a) for $\theta' = \pi/6$ and $\epsilon = 5 \times 10^{-4}$. (Initial position $\boldsymbol{\xi}_0$ is chosen to admit one-to-one comparison between simulated and experimental dynamics, Sec. III B). The tracer positions $\boldsymbol{\xi}_n$ in the first stage of the stroboscopic map $\mathcal{P}(\boldsymbol{\xi}_0)$ are indicated by black markers and delineate a thin shell centered on the chaotic sea in the original spheroid [Fig. 2(a), left], signifying similar dynamics as before. However, the second stage of the tracer evolution (magenta markers) involves a major departure from the unperturbed dynamics: the tracer enters (and periodically alternates between) a pair of tubes (emerging near the above-mentioned islands) and progressively migrates away from said spheroid. Basically any tracer on any spheroid delineates such tube-and-shell structures for arbitrary top-wall perturbation (θ', ϵ); alternative perturbation by weak fluid inertia via Re $\sim O(10^{-3}$–$10^{-2})$ has the same effect [12–14,20]. Moreover, an entirely different system, i.e., the above-mentioned magnetic-bead-driven microflow, also exhibits this behavior [15]. This implies that the physical topology of flows with spheroidal invariant surfaces generically consists of tube-and-shell structures as shown in Fig. 2(b).

Critical for the emergence of tube-and-shell structures is the coexistence of islands and chaotic seas of comparable size within the invariant spheroids so as to facilitate the formation of both tubes and shells upon perturbation. This requires intrasurface Hamiltonian dynamics in the unperturbed system sufficiently far away from the integrable state. Intrasurface topologies close to the integrable state, namely, consist predominantly of islands and upon perturbation thus "fail" to produce sizable chaotic shells necessary for tube-and-shell merger.

Nontoroidal invariant surfaces of greater topological complexity as well as quasi-2D representations of Lagrangian transport in geophysical flows accommodate similar Hamiltonian dynamics as shown in Fig. 2(a) [17–19]. This strongly suggests that the response to perturbation (including formation of tube-and-shell structures) demonstrated in Fig. 2(b) likely generalizes to a broader class of systems involving restriction of Lagrangian motion to (subregions of) nontoroidal invariant surfaces. Further exploration of this matter is beyond the present scope, however.

The phenomenon causing tube-and-shell structures is denoted "resonance-induced merger" due to its correlation with periodic lines, i.e., material curves of periodic points

$$\boldsymbol{\xi}_0 = \boldsymbol{\Phi}^p(\boldsymbol{\xi}_0), \tag{5}$$

that systematically return to their initial position after p periods, in the unperturbed flow topology [9,12–15]. The blue curve and green/yellow points in Fig. 2(b) indicate the periodic line and relevant degenerate points (specified in Sec. IV A), respectively, for shown instance of RIM. However, two key issues remain open. First, RIM has been explicitly demonstrated only in computational analyses; its physical existence is to date supported only by circumstantial experimental evidence [20]. Second, the underlying mechanisms remain elusive; existing theory relies on the emergence of isolated periodic points $\boldsymbol{\xi}_0$ according to (5) near perturbed periodic lines yet, though valid for an analogous flow and thus suspected here as well [15,20], fails to explain many instances of RIM in the cylinder flow (including that in Fig. 2). The current paper addresses these issues by (i) conclusive experimental proof of RIM and (ii) a comprehensive theory to explain the occurrence of RIM.

III. EXPERIMENTAL PROOF OF RIM

A. Long-term particle tracking

Experimental investigation of RIM involves direct measurement of the (evolution of) the tracer positions $\boldsymbol{\xi}_n$ of stroboscopic maps $\mathcal{P}(\boldsymbol{\xi}_0)$ following (3) by 3D particle-tracking velocimetry (3DPTV) using a modified version of the laboratory setup of [20] shown schematically (left) and in actuality

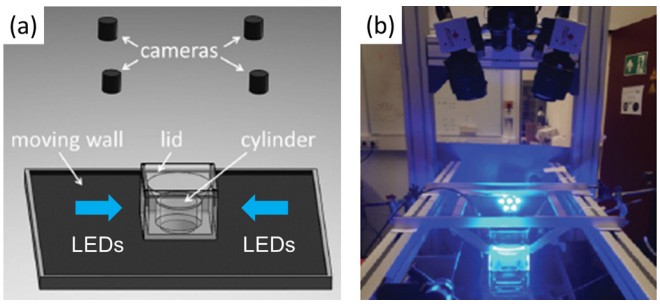

FIG. 3. Laboratory setup for measurement of stroboscopic maps using 3DPTV. (a) Schematic of the setup (adapted from [20]). (b) Actual setup.

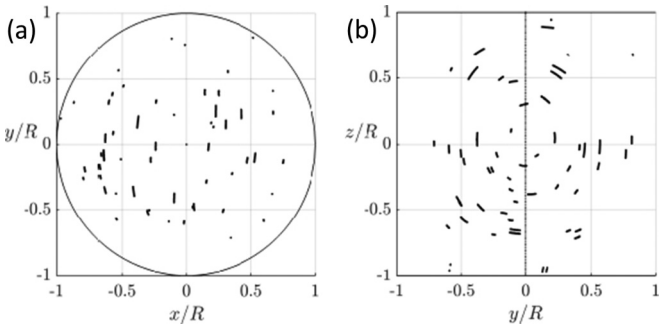

FIG. 4. Buoyancy-driven background circulation of magnitude $v \sim O$ (10^{-4} mm/s) due to a y-wise temperature drop $\Delta T \sim O(0.15$ K) as measured by 3DPTV. (a) Top view. (b) Side view.

(right) in Fig. 3. This setup incorporates the following key modifications (refer to [20] for other specifications). First, we employ high-viscosity silicon oil AK30000 by Wacker GmbH (kinematic viscosity $\nu = 0.03$ m^2/s, density $\rho = 970$ kg/m^3) for extremely close approximation of the Stokes limit (Re $\leqslant 6.6 \times 10^{-4}$). Second, we employ fluorescent polyethylene tracer particles (density $\rho_p = 1002$ kg/m^3, diameter $d_p =$ 75–90 μm) for enhanced imaging via fluorescence induced by illumination via two arrays of LEDs on either side of the test section [Fig. 3(a)]. Fluorescence, namely, yields a far greater intensity compared to conventional illumination and, by occurring at a color (red) different from the LEDs (blue), admits optical elimination of the background. This tremendously improves the tracking performance. Third, we implement an interactive module to the tracking algorithm for manual connection of segments of tracer paths upon visual inspection. Paths identified as separate entities, namely, often concern one tracer yet automated connection proves very difficult and unreliable. This interactive procedure, though laborious, gives a further significant improvement in tracking performance.

These modifications in conjunction with a low seeding density (around five particles per experiment) enable isolation of sufficiently long Lagrangian trajectories to expose RIM. Moreover, the relative settling velocity $U_p/U = |\rho_p - \rho| g d_p^2/18\rho\nu U \sim O(10^{-6})$ and Stokes number $\mathrm{St} = \rho_p d_p^2 U/18\rho\nu R \sim O(10^{-9})$ imply negligible effects of buoyancy and inertia, respectively, on the particle dynamics and thus indeed motion in accordance with passive tracers governed by kinematic equation (1).

B. Lagrangian dynamics in realistic flows

The experimental stroboscopic map $\mathcal{P}(\boldsymbol{\xi}_0)$ following (3) of a tracer released at the same position $\boldsymbol{\xi}_0$ as in Figs. 2(a) and 2(b) is shown in Fig. 2(c) and reveals a striking resemblance with the simulated perturbed state in Fig. 2(b) by revealing the same progression from a thin shell (black) into a pair of tubes (magenta). (The actual procedure is for practical reasons reversed: the simulated stroboscopic maps in Figs. 2(a) and 2(b) concern a tracer released at the same position $\boldsymbol{\xi}_0$ as in Fig. 2(c) [21]). Moreover, the experimental and numerical structures have a similar spatial extent and correlation with the simulated periodic line (blue). This is direct experimental proof of RIM and a physical topology in the present flow class that generically consists of corresponding tube-and-shell structures. These findings consolidate the hypothesis advanced in [20] that RIM, given explicit perturbation is absent, in the experiments results from natural disturbances and thus is inherent in realistic flows. The origin of these disturbances is established below.

Close proximity to the Stokes limit means Re is considerably below the range Re $\sim O(10^{-3}$–$10^{-2})$ for significant fluid inertia determined above and thus eliminates this as experimental perturbation for RIM. This furthermore implies that, given linearity of Stokes flows, the natural perturbation stems from a superimposed background flow due to a forcing other than the bottom wall (akin to e.g., the top-wall perturbation in the simulations). The 3DPTV for a stationary bottom wall indeed reveals a weak circulation (predominantly) parallel to the yz plane of magnitude $v \sim O(10^{-4}$ mm/s) as shown in Fig. 4 and suggests a buoyancy-driven flow. Temperature measurements expose a minute y-wise temperature drop $\Delta T \sim O(0.15$ K) due to (inevitably) imperfect ambient conditions that (upon verification by simulations in a 2D square cavity using a commercial CFD package) is consistent with such a circulation. The experimental perturbation is of strength $v/U \sim O(10^{-4})$ relative to the bottom-wall velocity $U \leqslant 1$ mm/s and thus is comparable to that of the simulations. This quantitatively supports the experimental proof of RIM. Moreover, given the perturbation has yet another origin, this further demonstrates that its particular nature is immaterial.

IV. TOWARDS A COMPREHENSIVE THEORY FOR RIM

The spheroidal invariant surfaces each accommodate at least one periodic point $\boldsymbol{\xi}_0$ following (5) on account of Brouwer's fixed-point theorem and the sets of points thus formed, by virtue of continuity, coalesce into periodic lines in the 3D domain. Hence such lines are inherent in the present flow class and computational analyses implicate these entities in RIM [9,12–14]. Thus the response of periodic lines to perturbation forms the basis for the comprehensive theory for RIM (including further experimental proof) developed below. This leans on expression of the Lagrangian dynamics near these entities in canonical forms that are valid under generic and universal conditions irrespective of the particulars of the flow system.

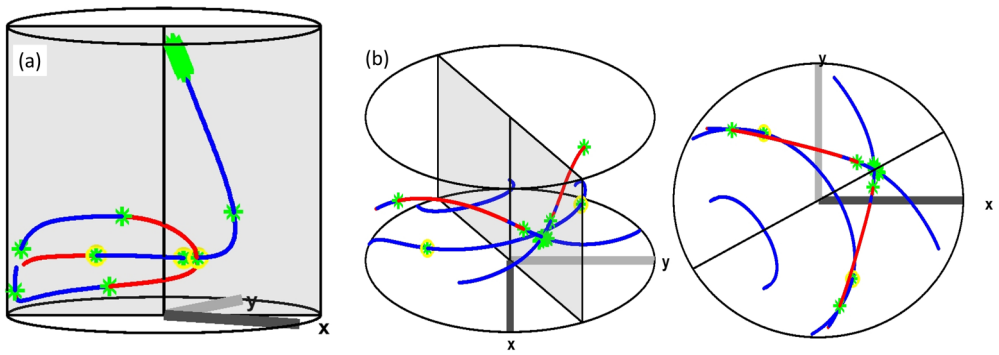

FIG. 5. Simulated periodic lines in time-periodic cylinder flow for Re = 0 and $D = 4$. (a) Periodic lines inside the symmetry plane. (b) Periodic lines outside the symmetry plane. Blue/red (dark/light gray), elliptic/hyperbolic (segments of) periodic lines; green star and green star/yellow circle, degenerate points for $\alpha_p = 2$ and -2, respectively; shaded plane (perspective view)/tilted line (top view), symmetry plane $\Theta = \pi/6$.

A. Canonical dynamics near periodic lines

Periodic lines in the time-periodic cylinder flow (Re = 0 and $D = 4$ as before) consisting of periodic points following (5) for $p = 1$ and 2 are given in Fig. 5 and hereafter denoted period-1 and period-2 lines, respectively. These lines are arranged relative to a symmetry plane $\Theta = \pi/6$ (shaded); they either coincide with or are reflected about the latter according to Fig. 5(b) [14]. (Physical existence of periodic lines is demonstrated experimentally in [20,22]). The highlighted segments and points distinguish essentially different local dynamics and such segmentation is typical of periodic lines and crucial to the response to perturbations. Characterization of the line segments embarks on expression of mapping (2) in canonical form via its local linearization

$$\boldsymbol{\xi}'_{n+1} = \boldsymbol{\mathcal{F}}_0 \boldsymbol{\xi}'_n, \quad \boldsymbol{\mathcal{F}}_0 = \left.\frac{\partial \boldsymbol{\Phi}_0}{\partial \boldsymbol{\xi}}\right|_{\boldsymbol{\xi}_0}, \tag{6}$$

with $\boldsymbol{\xi}' = \boldsymbol{\xi} - \boldsymbol{\xi}_0$ the local Cartesian reference frame at a periodic point $\boldsymbol{\xi}_0$ on the periodic line and $\boldsymbol{\mathcal{F}}_0$ the deformation tensor for mapping $\boldsymbol{\Phi}_0$ (subscript "0" indicates unperturbed conditions). The dynamics in the eigenspace $\boldsymbol{x}$ of $\boldsymbol{\mathcal{F}}_0$ are described by the canonical map

$$\boldsymbol{x}_{n+1} = \boldsymbol{F}_0 \boldsymbol{x}_n, \tag{7}$$

with $\boldsymbol{F}_0$ a linear operator that admits two nondegenerate cases discriminated by

$$\alpha = \mathrm{tr}(\boldsymbol{\mathcal{F}}_0) - 1, \tag{8}$$

and corresponding with

$$\boldsymbol{F}_0(\alpha) = \begin{bmatrix} \lambda & 0 & 0 \\ 0 & \lambda^{-1} & 0 \\ 0 & 0 & 1 \end{bmatrix}, \quad \boldsymbol{F}_0(\alpha) = \begin{bmatrix} c & -s & 0 \\ s & c & 0 \\ 0 & 0 & 1 \end{bmatrix}, \tag{9}$$

for $|\alpha| > 2$ and $|\alpha| < 2$, respectively, with coefficients

$$\lambda(\alpha) = \frac{\alpha}{2} + \sqrt{\left(\frac{\alpha}{2}\right)^2 - 1}, \quad c(\alpha) = \cos\mu = \frac{\alpha}{2}, \tag{10}$$

and $s = \sin\mu = \sqrt{1 - c^2}$. Here z axis and planes $z = \text{const}$ represent the periodic line and spheroidal invariant surfaces, respectively, in canonical space $\boldsymbol{x}$. These planes correspond with coordinate surfaces $\zeta_3 = \text{const}$ of the curvilinear reference frame $\boldsymbol{\zeta}$ adopted for the Hamiltonian representation (4) of the system in physical space. The planar motion in (x, y) directions corresponds with the local intrasurface Hamiltonian dynamics in (ζ_1, ζ_2) directions near the periodic line in question. Refer to Appendix A for a detailed discussion.

Discriminant (8) generically varies along a given periodic line, meaning that these entities are in canonical space characterized by a line-specific relation

$$\alpha = \alpha(z), \tag{11}$$

which determines the unperturbed dynamics according to (7) by a canonical operator (9) dependent on the local line properties via $\boldsymbol{F}_0[\alpha(z_n)]$. Thus $\alpha = \alpha(z_n)$ governs the local planar dynamics in the invariant surfaces $z = \text{const}$ as follows (colors refer to Fig. 5): hyperbolic orbits

$$(x_{n+1}, y_{n+1}) = (\lambda x_n, y_n/\lambda) \tag{12}$$

for $|\alpha| > 2$ (red) and circular concentric orbits

$$(r_{n+1}, \vartheta_{n+1}) = (r_n, \vartheta_n + \mu) \tag{13}$$

for $|\alpha| < 2$ (blue), with (r, ϑ) standard polar coordinates following $(x, y) = (r\cos\vartheta, r\sin\vartheta)$ and coefficients (λ, μ) given by (10). Line segments yielding (12) and (13) are denoted "hyperbolic" and "elliptic," respectively, and are separated by degenerate points $\widetilde{z}$ defined implicitly as

$$\alpha(\widetilde{z}) = \alpha_p = \pm 2, \tag{14}$$

and termed "parabolic points." The periodic lines in Fig. 5 accommodate such parabolic points both for $\alpha_p = 2$ (green) and $\alpha_p = -2$ (green/yellow). Moreover, the unstable (stable) manifold of hyperbolic line segments coincides in each invariant surface $z = \text{const}$ with the $x(y)$ axis and $y(x)$ axis for $\alpha_p > 2$ and $\alpha_p < -2$, respectively.

Existence of the above relations relies solely on continuity and solenoidality of flow $\boldsymbol{u}$ underlying mapping (2). Thus the canonical form is valid for periodic lines in basically any flow subject to incompressibility. This generality and universality extends to the perturbed canonical mapping introduced below that derives from this form.

B. Canonical dynamics for perturbed conditions

Arbitrary perturbation extends canonical map (7) to

$$\boldsymbol{x}_{n+1} = \boldsymbol{F}\boldsymbol{x}_n + \boldsymbol{d}, \tag{15}$$

with the operator $\boldsymbol{F}$ to leading order given by

$$\boldsymbol{F} = \begin{bmatrix} A\lambda & 0 & 0 \\ 0 & \frac{B}{\lambda} & 0 \\ 0 & 0 & C \end{bmatrix}, \quad \boldsymbol{F} = \begin{bmatrix} \frac{c'}{\sqrt{C}} & -\frac{s'}{\sqrt{C}} & 0 \\ \frac{s'}{\sqrt{C}} & \frac{c'}{\sqrt{C}} & 0 \\ 0 & 0 & C \end{bmatrix}, \tag{16}$$

for $|\alpha| > 2$ and $|\alpha| < 2$, respectively, with $C = 1/AB$ and

$$c' = \cos\mu' = \frac{(A+B)\cos\mu}{2\sqrt{AB}} = \sqrt{1-s'^2}, \tag{17}$$

where coefficients (λ, μ) are following (10). The additional coefficients $(A, B) = (1+a, 1+b)$ affect the deformation characteristics of the unperturbed state via $a = b = \epsilon_1$ (equality permitted without loss of generality unless stated otherwise) and vector

$$\boldsymbol{d} = (0, 0, \epsilon_2) \tag{18}$$

introduces a z-wise background drift normal to the invariant surfaces. Thus parameters $|\epsilon_{1,2}| \ll 1$ control the perturbation of a periodic line characterized by a given discriminant $\alpha = \alpha(z)$ following (11); canonical map (15) identifies with its unperturbed counterpart (7) for $\epsilon_1 = \epsilon_2 = 0$. Refer to Appendix B for derivation and parametrization of perturbed map (15).

Canonical map (15) has an isolated periodic point

$$\boldsymbol{x}_* = (\boldsymbol{I} - \boldsymbol{F})^{-1}\boldsymbol{d} = (0, 0, z_*), \quad z_* = \frac{\epsilon_2}{1-C}, \tag{19}$$

and thus admits distinction of two relevant cases: presence and absence of (an) isolated periodic point(s) in the domain of interest. Presence can be represented by $\boldsymbol{x}_* = \boldsymbol{0}$ via $z_* = 0$ ($\epsilon_2 = 0$); absence can be represented by placement of $\boldsymbol{x}_*$ outside said domain via $|z_*| \gg 1$.

The general impact of perturbations on the dynamics near periodic lines, assuming absence of a periodic point $\boldsymbol{x}_*$ following (19), is determined by operator $\boldsymbol{F}$. Comparing (9) and (16) reveals that $\boldsymbol{F}$ retains the structure of $\boldsymbol{F}_0$, implying that the basic nature of the dynamics is preserved. The perturbed xy-wise orbits shadow the unperturbed ones and remain hyperbolic and elliptic for $|\alpha| > 2$ and $|\alpha| < 2$, respectively. The fundamental departure from the unperturbed state exists in the emergence of a z-wise drift $z_{n+1} - z_n \approx \epsilon_2$ for arbitrary nonzero ϵ_2 and the inherent breakdown of the invariant surfaces $z = \text{const}$, which manifests itself in dramatically different ways for hyperbolic versus elliptic lines.

For hyperbolic lines, significant planar motion parallel to the original invariant surface for regime $\alpha > 2$ is in the x direction and relates to the corresponding normal drift following

$$\frac{x_{n+1} - x_n}{z_{n+1} - z_n} = \gamma_h x_n, \quad \gamma_h \approx \frac{\lambda - 1}{\epsilon_2}, \quad \gamma_h \gg 1, \tag{20}$$

implying a rapid x-wise divergence from the unperturbed periodic line before an appreciable z-wise drift can develop (Appendix C1). Likewise behavior occurs in the y direction for regime $\alpha < -2$. Hence planar motion along the unstable manifold dominates over the normal drift and, in consequence, confines tracers to a thin shell around the chaotic sea of the corresponding invariant surface. Thus the perturbation has an only marginal impact on the dynamics near hyperbolic lines.

For elliptic lines, on the other hand, planar (radial) motion parallel to the original invariant surface is relatively weak, i.e.,

$$\frac{r_{n+1} - r_n}{z_{n+1} - z_n} = \gamma_e r_n, \quad \gamma_e \approx \frac{1-\sqrt{C}}{\sqrt{C}\epsilon_2}, \quad |\gamma_e| \ll 1, \tag{21}$$

implying prolonged (radial) entrapment near the original periodic line in conjunction with an appreciable drift normal to the unperturbed invariant surface (Appendix C2). Thus the perturbation, in contrast with their hyperbolic counterparts, has a major impact on the dynamics near elliptic lines. Here this induces helical motion around the z axis and transverse to the original invariant surfaces along invariant tubes [for any $|\alpha(z)| < 2$] parametrized by

$$G(r, z) = r^2(z - z_*), \tag{22}$$

and approximately of constant radius for $|z_*| \gg 1$. Relation (22) follows from (15) and (16) upon elimination of ϵ_2 via (19) and expression of planar motion in polar coordinates. This gives $C = r_n^2/r_{n+1}^2 = (z_{n+1} - z_*)/(z_n - z_*)$ and implies a constant of motion $G(r_{n+1}, z_{n+1}) = G(r_n, z_n)$ and, inherently, tubular invariant surfaces described by its level sets. Both the radial and normal displacements scaling (reciprocally) with coefficient C stem from condition $\det(\boldsymbol{\mathcal{F}}) = \det(\boldsymbol{F}) = 1$ and thus incorporate the solenoidality of flow $\boldsymbol{u}$ underlying mapping (2).

The drift normal to the original invariant surfaces occurs for any perturbation and thus causes the physical topology to generically consist of chaotic shells and tubes instead of chaotic seas and islands within (spheroidal) invariant surfaces. Moreover, these structures, rather than coexisting, merge into tube-and-shell structures as shown in Figs. 2(b) and 2(c) by RIM.

Resonances in the angular motion are key to RIM by enabling the escape of tracers from tubes (into a chaotic environment) through interruption of the so-called averaging principle that underlies the survival of tubes under weak perturbation [4]. Such resonances—and resulting escapes—are widely studied yet exclusively for local defects in tubes on fully elliptic lines (i.e., case $|\alpha| < 2$ of the canonical map). Generalize to this end the spatial variation of the periodwise angular displacement in (13) from $\mu(z_n) = \mu(z_0)$, ensuing from (9) and (11), to $\mu = \mu(r_n, z_n) = \mu(r_0, z_0)$ (which is necessary only to capture local resonances). Local defects due to resonances occur if the angular displacement becomes commensurate with 2π in certain curves in the rz plane, i.e.,

$$\mu(r, z) = 2\pi k/m, \tag{23}$$

with (k, m) arbitrary integers, where the surfaces of revolution described by the curves are termed "resonance sheets." This triggers either random switching between tubes (denoted "resonance-induced dispersion" or "scattering") near the resonance sheets or prolonged oscillation around the latter ("capture into resonance") [5–7].

RIM, instead of local defects through resonances (23), involves full truncation of such tubes and depends solely on the properties of the periodic line characterized by discriminant $\alpha = \alpha(z)$ following (11). The canonical map enables distinction of three truncation scenarios and thus yields a comprehensive theory that (as opposed to current theories) explains *all* instances of RIM. Two of these scenarios involve resonance phenomena due to commensurate μ following (23) yet for describing full tube truncations necessitate only $\mu = \mu(z)$ via (11). Moreover, the canonical map enables demonstration that RIM indeed involves merger *of* (instead of random switching *between*) Lagrangian entities. This comprehensive theory is elaborated below.

The (un)perturbed canonical map is nonlinear via the dependence of discriminant (11) in operator $\boldsymbol{F}_0$ in (7)—and thus also $\boldsymbol{F}$ in (15)—on the normal coordinate z yet with a special structure in that the dynamics are (according to conventional perturbation theory) linear in the planar coordinates (x, y) within an invariant surface $z = \text{const}$. Thus the canonical map can adequately capture the local (perturbed) dynamics associated with a given periodic line with arbitrary characteristics including segmentation.

Possible perturbation-induced nonlinear interactions with entities of nearby periodic lines, particularly between chaotic trajectories around a hyperbolic line segment and islands on neighboring elliptic lines, are beyond the perturbed canonical map. However, the premise of intrasurface Hamiltonian dynamics in the unperturbed system sufficiently far away from the integrable state (Sec. II B) strongly diminishes (or even precludes) such islands in a chaotic sea. Thus corresponding nonlinear interactions generically are (if existent at all) highly localized in the flow regime relevant for RIM.

C. RIM due to formation of periodic points

The first RIM scenario hinges on the formation of an isolated periodic point $\boldsymbol{x}_*$ following (19) near a perturbed elliptic line ($|\alpha| < 2$), which can be identified with the origin without loss of generality (Sec. IV B). The local dynamics around $\boldsymbol{x}_*$ are described by map (15) for $|\alpha| < 2$ and $\epsilon_2 = 0$ and (consistent with findings in [6]) retain the nature of the elliptic line in that tracers perform helical motion—describing tubes—around the associated one-dimensional (1D) manifold W_{1D} (z axis). However, contrary to cases devoid of periodic points, the z-wise drift reverses on either side of the associated 2D manifold W_{2D} (plane $z = 0$). The z-wise motion in the perturbed map (15), namely, simplifies to $z_{n+1} = Cz_n$ for $\epsilon_2 = 0$ and thus gives rise to

$$z_{n+1} > z_n \text{ for } z_n > 0 \text{ and } z_{n+1} < z_n \text{ for } z_n < 0,$$

for $C > 1$. Case $C < 1$ yields the opposite dynamics, i.e.,

$$z_{n+1} < z_n \text{ for } z_n > 0 \text{ and } z_{n+1} > z_n \text{ for } z_0 < 0,$$

and causes the helical paths to diverge upon approaching W_{2D} as illustrated in Fig. 6 by the stroboscopic map (left) of a tracer (black) released at $\boldsymbol{x}_0 = (0.2, 0.2, -2)$ (red) below W_{2D} (gray) of $\boldsymbol{x}_*$ (magenta) using $\alpha = 0.2$ in Fig. 6 (right) as characteristic discriminant $\alpha(z)$ following (11) ($\epsilon_1 = 10^{-3}$, $\epsilon_2 = 0$). Thus W_{2D} truncates the tubes into two families of

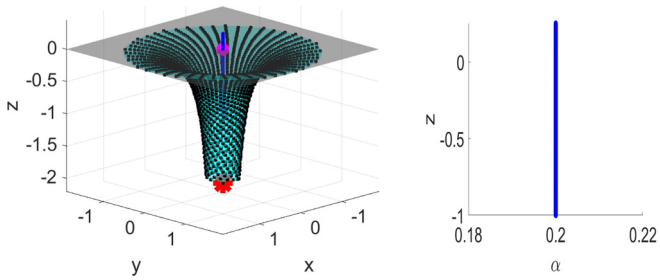

FIG. 6. Tube-shell merger (left) due to formation of isolated periodic point $\boldsymbol{x}_*$ (magenta sphere) near the elliptic line (blue), characterized by $|\alpha(z)| < |\alpha_p| = 2$ (right), demonstrated by the perturbed canonical map (left) of a single tracer (black, time progression upwards) released at $\boldsymbol{x}_0$ (red star). Gray horizontal plane, W_{2D} of $\boldsymbol{x}_*$; cyan funnel, invariant surfaces describing tube-and-shell structures.

funnel-shaped invariant surfaces parametrized by (22) for $z_* = 0$ (cyan).

The above RIM scenario occurs in the magnetic-bead-driven flow in [15] and is, by analogy, also attributed to RIM in the cylinder flow [20]. However, computational studies reveal that the instances of RIM observed in this system (including Fig. 2) are in fact devoid of periodic points and thus beyond the associated theory in [15] (which is based on [6]). This includes instances of RIM in [15] due to the sudden deflection of 1D manifolds W_{1D} (upon which tubes are centered) into chaotic shells at locations without other periodic points.

The absence of periodic points lends further credence to an essentially different RIM scenario suggested in [12–14] (and its name giver): tube-shell merger induced by resonances in the dynamics associated with the periodic line. RIM occurs according to this scenario near positions z on the periodic line where the angular displacement $\mu = \mu(z)$ following (10) satisfies condition (23). This hypothesis is validated hereafter by theoretical analysis and experimental proof and advances two further scenarios: RIM due to local and global segmentation of periodic lines (Sec. V). This furthermore demonstrates that RIM indeed involves merger of Lagrangian entities—instead of random switching reminiscent of "resonance-induced dispersion" or "scattering" (Sec. IV B)—by exposing the existence of invariant surfaces that smoothly extend from the tubes into the chaotic shells (Sec. VI). Thus existing theory, holding only for RIM due to isolated periodic points, is expanded to a comprehensive theory for *all* instances of RIM.

V. RIM DUE TO SEGMENTATION OF PERIODIC LINES

A. Resonances on periodic lines

The resonance phenomena described in Sec. IV B interrupt the averaging principle that underlies the survival of tubes under weak perturbation and thus causes local defects in these entities [4–7]. RIM involves an essentially different resonance phenomenon that concerns the transition between elliptic and hyperbolic dynamics according to (12) and (13), respectively. Regions with former and latter dynamics, namely, join at invariant surfaces $z = \text{const}$ in which discriminant $\alpha(z)$ following (11) identifies with the parabolic limit (14) and yields

an angular displacement $\mu = \mu(z)$ through (10) that satisfies condition (23). This gives two distinct cases.

(1) Case $\alpha(\widetilde{z}) = \alpha_p = 2$ yields $\mu(\widetilde{z}) = 0$ and corresponding coefficient $\lambda(\widetilde{z}) = 1$. Both (12) and (13) collapse on $(x_{n+1}, y_{n+1}) = (x_n, y_n)$, implying an invariant surface $\widetilde{z} =$ const consisting entirely of period-1 points.

(2) Case $\alpha(\widetilde{z}) = \alpha_p = -2$ yields $\mu(\widetilde{z}) = \pi$ and corresponding coefficient $\lambda(\widetilde{z}) = -1$. Here (12) and (13) collapse on $(x_{n+1}, y_{n+1}) = (-x_n, -y_n)$, implying $(x_{n+2}, y_{n+2}) = (x_n, y_n)$ and thus an invariant surface $\widetilde{z} =$ const consisting entirely of period-2 points.

Thus resonances underlying RIM are in essence special cases of (23) in that the resonance sheets identify with invariant surfaces $z =$ const. These sheets in principle cause the same defects in tubes as in the resonance phenomena following Sec. IV B yet their impact on the dynamics, notwithstanding this similarity, is fundamentally different. First, the resonance sheets thus formed, akin to the 2D manifold associated with RIM due to periodic points (Sec. IV C), fully truncate the tubes instead of causing only local defects. Second, these sheets, given their emergence on the boundary between elliptic and hyperbolic line segments, facilitate the migration of tracers into chaotic shells and vice versa. This gives rise to two further RIM scenarios complementary to that following Sec. IV C: RIM due to local and global segmentation of periodic lines into elliptic and hyperbolic segments. This is elaborated in Secs. V B and Sec. V C, respectively. Section V D expands the scope of RIM due to local segmentation by demonstrating that this scenario in fact includes periodic lines consisting entirely of elliptic segments separated by parabolic points.

B. Local segmentation

Local segmentation may occur near parabolic points $\widetilde{z}$ following (14) on elliptic periodic lines as indicated by green and blue, respectively, in Fig. 2(b). Such points are accompanied by small line segments that approach the parabolic limit $\alpha = \alpha_p = \pm 2$ up to a tolerance $\Delta \ll 1$ and any sections within this tolerance for which

$$|\alpha_p| < |\alpha| \leqslant |\alpha_p| + \Delta \tag{24}$$

demarcate small weakly hyperbolic segments on an otherwise elliptic line. [Green markers in Fig. 2(b) in fact delineate line segments within tolerance $\Delta = 5 \times 10^{-3}$.] The impact of such local segmentation on the perturbed dynamics without periodic points admits representation by map (15) using $\epsilon_2 > 0$ and discriminant

$$\alpha(z) = \gamma|z| + \beta, \quad |\beta| > |\alpha_p| = 2, \tag{25}$$

yielding a weakly hyperbolic segment following (24) for $\Delta = |\beta| - 2$ and bounded by parabolic points $\widetilde{z} = \pm\Delta/\gamma$. Figures 7(a) and 7(b) demonstrate the two possible cases $\alpha_p = 2$ and -2, respectively, identified in Sec. V A by the stroboscopic map (left) of a tracer released at $\boldsymbol{x}_0 = (1, 1, -1)$ and characterized by shown discriminant $\alpha(z)$ (right) for $(\epsilon_1, \epsilon_2) = (10^{-5}, 10^{-3})$ and $(\gamma, \beta) = (\pm 0.5, \mp 2.01)$ (yielding $z_* = 50$ and $\widetilde{z} = \pm 0.02$): (i) deflection of a single orbit from the tube on the lower elliptic segment (blue) along the unstable manifold (dark gray) of the hyperbolic segment (red) for $\beta = 2.01$ upon crossing resonance sheet $\widetilde{z} = -0.02$ corresponding with parabolic limit $\alpha(\widetilde{z}) = \alpha_p = 2$ and (ii) emergence of two deflected orbits for $\beta = -2.01$ upon crossing the resonance sheet $\widetilde{z} = -0.02$ corresponding with

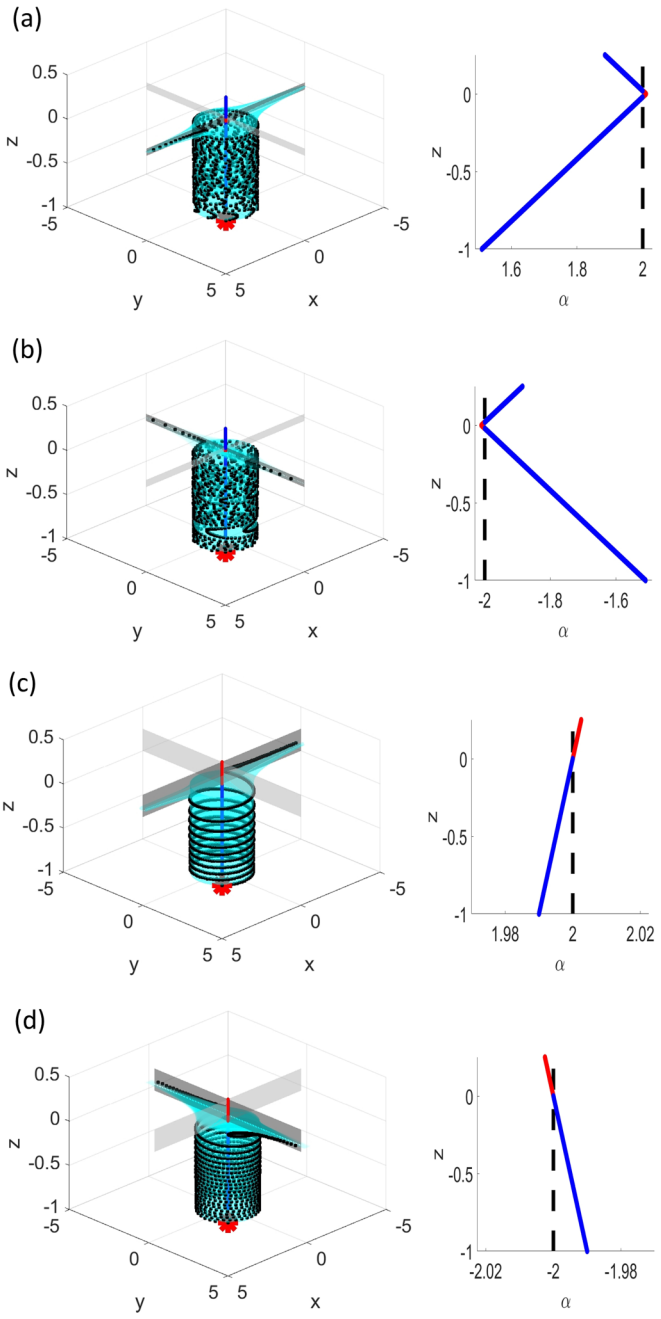

FIG. 7. Tube-shell merger due to segmentation of periodic lines demonstrated by the perturbed canonical map (left) of a single tracer (black, time progression upwards) released at $\boldsymbol{x}_0$ (red star) near the periodic line (vertical axis; blue/red, (dark/light gray) elliptic/hyperbolic) characterized by $\alpha(z)$ (right). (a) Local segmentation for $\alpha_p = 2$. (b) Local segmentation for $\alpha_p = -2$. (c) Global segmentation for $\alpha_p = 2$. (d) Global segmentation for $\alpha_p = -2$. Dashed line in $\alpha(z)$, parabolic limit $\alpha_p = \pm 2$; light/dark gray vertical planes, stable/unstable manifolds of the hyperbolic line segment; cyan, diverging upright cylinders, invariant surfaces describing tube-and-shell structures.

parabolic limit $\alpha(\widetilde{z}) = \alpha_p = -2$. Single versus double orbit(s) occur due to period-1 ($\mu(\widetilde{z}) = 0$) versus period-2 ($\mu(\widetilde{z}) = \pi$) resonance, respectively, at given parabolic limits according to Sec. V A.

Lagrangian motion is in the perturbed map restricted to newly formed invariant surfaces indicated in cyan for shown tracers in Figs. 7(a) and 7(b) that are topologically equivalent to the funnel-shaped invariant surfaces in Fig. 6 for the RIM scenario according to Sec. IV C. This implies that RIM, as opposed to random dispersion due to resonance-induced defects in tubes, indeed merges tubes and shells. The origin and structure of these invariant surfaces are elaborated in Sec. VI. Furthermore, Sec. V D demonstrates that RIM due to local segmentation includes periodic lines consisting entirely of elliptic segments separated by parabolic points.

C. Global segmentation

Global segmentation involves, instead of small weakly hyperbolic segments following (24) on an otherwise elliptic line, hyperbolic and elliptic segments of similar extent. Consider to this end map (15) for discriminant

$$\alpha = \gamma z + \beta, \quad \beta = \alpha_p = \pm 2, \tag{26}$$

partitioning the periodic line into an elliptic ($z < 0$) and hyperbolic ($z > 0$) segment at parabolic point $\widetilde{z} = 0$. Figures 7(c) and 7(d) demonstrate the two possible cases $\alpha_p = \pm 2$ (Sec. V A) by a tracer released at $\boldsymbol{x}_0 = (1, 1, -1)$ for $(\epsilon_1, \epsilon_2) = (10^{-5}, 10^{-3})$ and $\gamma = 0.01$ ($z_* = 50$): deflection of a single and pair of orbit(s) from the tube on the elliptic segment (blue) along the unstable manifold (gray) of the hyperbolic segment (red) for $\alpha(\widetilde{z}) = \alpha_p = 2$ and -2, respectively. Again, cases $\alpha_p = \pm 2$ distinguish period-1 versus period-2 resonances (Sec. V A) and Lagrangian motion is restricted to invariant surfaces (cyan).

Thus global segmentation basically yields dynamics comparable to that ensuing from local segmentation. The difference between former and latter primarily exists in the extent and interaction of the associated invariant surfaces and their impact on the dynamics. This is elaborated in Sec. VI.

D. Local segmentation revisited

Behavior equivalent to that ensuing from local segmentation of periodic lines following Sec. V B occurs near parabolic points on otherwise entirely elliptic lines. The dynamics on line segments close to the parabolic limit $\alpha_p = \pm 2$, demarcated by a discriminant

$$\alpha_{\min} \leqslant |\alpha| \leqslant |\alpha_p|, \quad \alpha_{\min} = \frac{4\sqrt{AB}}{A+B} \leqslant |\alpha_p|, \tag{27}$$

namely, undergoes a qualitative change from *elliptic unperturbed* dynamics governed by operator $\boldsymbol{F}_0$ (right) in (9) to *hyperbolic perturbed* dynamics governed by operator $\boldsymbol{F}$ (left) in (16) (Appendix D). Thus a periodic line partitioned only into elliptic segments by parabolic points yields perturbed dynamics essentially similar as for "actual" local segmentation in that line segments meeting (27) cause the same behavior as local hyperbolic segments following (24). This implies a "virtual local segmentation" of the elliptic line near parabolic points.

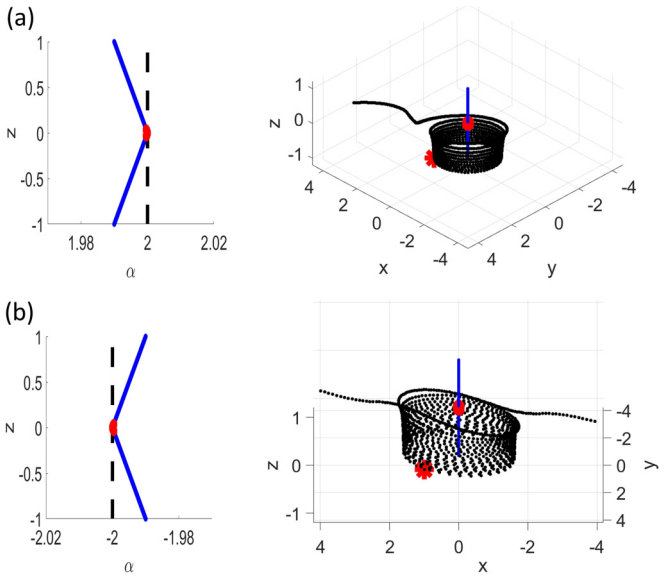

FIG. 8. Tube-shell merger due to virtual local segmentation of the elliptic periodic line (right; vertical axis) characterized by $\alpha(z)$ (left) with the parabolic point at $\widetilde{z} = 0$ demonstrated by the perturbed canonical map (right) of a single tracer (black, time progression upwards) released at $\boldsymbol{x}_0$ (red star). (a) $\alpha_p = 2$. (b) $\alpha_p = -2$. Dynamics near blue (dark gray) and red (light gray) line segments remains elliptic and becomes hyperbolic, respectively, upon perturbation. Dashed line in $\alpha(z)$, parabolic limit $\alpha_p = \pm 2$.

Property $\alpha_{\min} < |\alpha_p|$ for any perturbation $a \neq b$ means that virtual local segmentation is generic and basically always happens for some finite line segment near parabolic points on an elliptic line (Appendix D). (Note that, unlike the other response scenarios, inequality $a \neq b$ is essential here). However, such line segments—and thus local emergence of hyperbolic dynamics—are confined to the direct proximity of said points; significant perturbation $|a, b| \approx 0.1$ gives an only minute departure $\alpha_{\min} \approx 1.99$ from the parabolic limit. (Refer to Fig. 14 for a full visualization of $\alpha_{\min}$ versus the perturbation strength). Hence the discriminant on an elliptic line, save these localized regions near parabolic points, meets $\alpha < \alpha_{\min}$ and the perturbed dynamics generically retains the elliptic nature of the unperturbed state.

Consider an elliptic line characterized by a discriminant $\alpha(z) \leqslant 2$ following (25), with $\gamma = -0.01$ and $\beta = \alpha_p = 2$, partitioned by a parabolic point $\widetilde{z} = 0$ [Fig. 8(a), left]. Perturbation $a = -b = \epsilon_1$ and drift $\boldsymbol{d}$ following (18), with $(\epsilon_1, \epsilon_2) = (0.02, 10^{-3})$, yields $\alpha_{\min} = 1.9996$ and a line segment $-\widetilde{z}_* \leqslant z \leqslant \widetilde{z}_*$, with

$$\widetilde{z}_* = (\alpha_{\min} - \beta)/\gamma = 0.0392, \tag{28}$$

meeting condition (27). This implies virtual local segmentation and the perturbed dynamics in Fig. 8(a) (right) of a tracer (black) released at $\boldsymbol{x}_0 = (1, 1, -1)$ (red) indeed exhibits the same deflection from the periodic line upon approaching line segment $|z| \leqslant \widetilde{z}_*$ (highlighted in red) as found for actual local segmentation in case of $\alpha_p = 2$ in Fig. 7(a). Similar equivalence occurs for case $\alpha_p = -2$; compare to this end Fig. 8(b) with Fig. 7(b).

An important (quantitative) difference between actual and virtual local segmentation is that the latter constitutes a far weaker mechanism. Similar discriminant and perturbation as for the local segmentation in Fig. 7(a), namely, yield $|\alpha_p| - \alpha_{\min} \sim O(10^{-10})$ and $\widetilde{z}_* \sim O(10^{-9})$, signifying a negligible effect. Thus sufficiently strong perturbation, i.e., "large" departures of (A, B) in (27) from unity, and sufficiently flat profiles for the discriminant near parabolic points, i.e., "small" γ in (28), are imperative for a significant impact by virtual segmentation.

Both actual local and global segmentation strictly also involve virtual local segmentation in that the dynamics near portions of the elliptic line segment(s) adjacent to the hyperbolic segment meeting (27) become hyperbolic upon perturbation. However, this only slightly shifts the separation between perturbed elliptic and hyperbolic dynamics from the parabolic point $|\alpha_p| = 2$ to $|\alpha| = \alpha_{\min}$ and otherwise is inconsequential for the corresponding RIM scenarios. Moreover, the relative weakness of RIM due to virtual local segmentation established above renders this shift negligible for perturbation strengths typical of RIM due to local and global segmentation.

E. Typical manifestations of RIM in realistic flows

The response scenarios developed in Secs. V A–V D enable explanation of the instance of RIM shown in Figs. 2(b) and 2(c). The fact that the tube-shell merger occurs near a parabolic point $\alpha_p = -2$ (green/yellow marker) on an otherwise entirely elliptic periodic line (blue curve) implies virtual local segmentation according to Fig. 8(b) as underlying mechanism. Further investigation reveals that tubes smaller than those in Fig. 2 tend to continue past the parabolic point by randomly switching between tube segments on either side of the hyperbolic region (not shown) reminiscent of "scattering" following [7]. This reflects the relative weakness of RIM due to virtual local segmentation pointed out in Sec. V D and suggests that for this scenario typically only the outer tubes sufficiently close to the surrounding chaotic sea exhibit global behavior according to Figs. 2(b) and 2(c). The switching between the inner tubes nonetheless involves a highly localized manifestation of RIM in that tracers cross over via a thin hyperbolic layer separating two tube families (Sec. VI). This is demonstrated below for another instance of RIM.

Further manifestations of RIM in the cylinder flow due to the segmented periodic lines in Fig. 5 are shown in the simulated stroboscopic map of a single tracer in Fig. 9(a). Parabolic points I–III and IV concern actual ($\alpha_p = -2$) and virtual ($\alpha_p = 2$) segmentation, respectively, and time progression is from IV to I. The dynamics at points I–III are, similar to Fig. 2, entirely consistent with the canonical behavior in Figs. 7(a)–7(d) corresponding with actual segmentation of periodic lines into elliptic and hyperbolic parts. Point I separates elliptic and hyperbolic segments of comparable extent and thus corresponds with global segmentation. However, the close proximity of points II and III induces behavior characteristic of local segmentation by resulting in nontrivial interaction between the perturbed dynamics near the separated elliptic segments: the tracer randomly switches between the invariant surfaces associated with both instances of RIM (cyan in Fig. 7) and thus effectively crosses over from one tube segment into another via the intermediate hyperbolic region. Figure 9(b) gives the corresponding experimental stroboscopic map (and simulated periodic line) and its close agreement with Fig. 9(a) provides further experimental proof of the physical existence and universality of RIM due to segmentation of periodic lines.

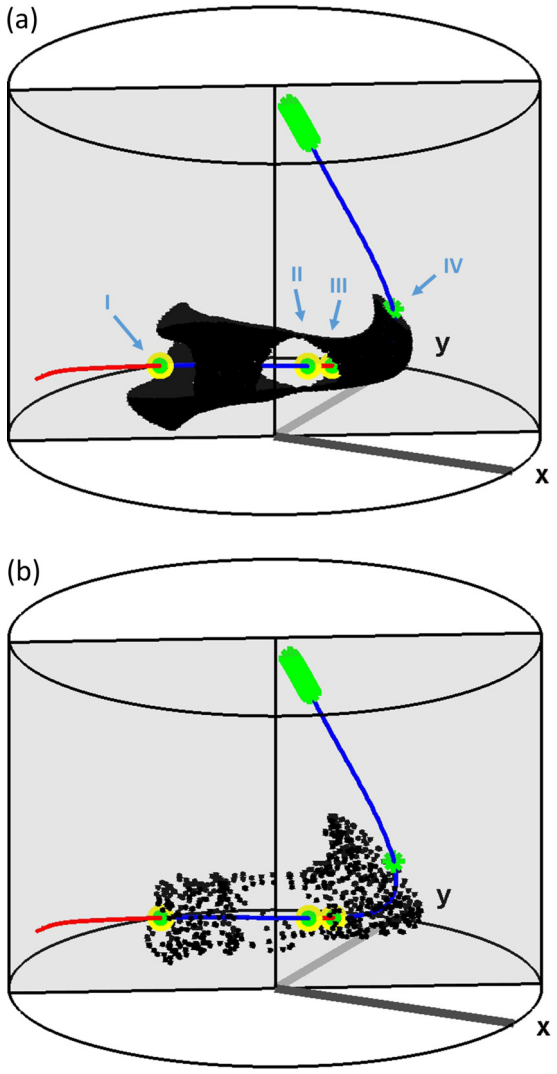

FIG. 9. Manifestations of RIM in cylinder flow due to segmented periodic lines (color coding and labeling as before) demonstrated by the stroboscopic map of a single tracer. (a) Simulated map. (b) Experimental map. Parabolic points I–III and IV concern actual ($\alpha_p = -2$) and virtual ($\alpha_p = 2$) segmentation, respectively; time progression is from IV to I.

Figure 10(a) shows the continuation of the simulated stroboscopic map of the single tracer in Fig. 9(a) at parabolic points I (cyan) and IV (magenta) forward and backward in time, respectively. The tracer beyond point I clearly migrates from the tube segment into a chaotic shell and thus supports the above finding of RIM due to global segmentation. The experimental stroboscopic map of a nearby tracer in Fig. 10(b) exposes a similar chaotic shell and its coincidence with the simulated chaotic shell demonstrated in Fig. 10(c) (cyan versus blue) physically validates the location and extent of this shell and thus, indirectly, further validates this instance of RIM.

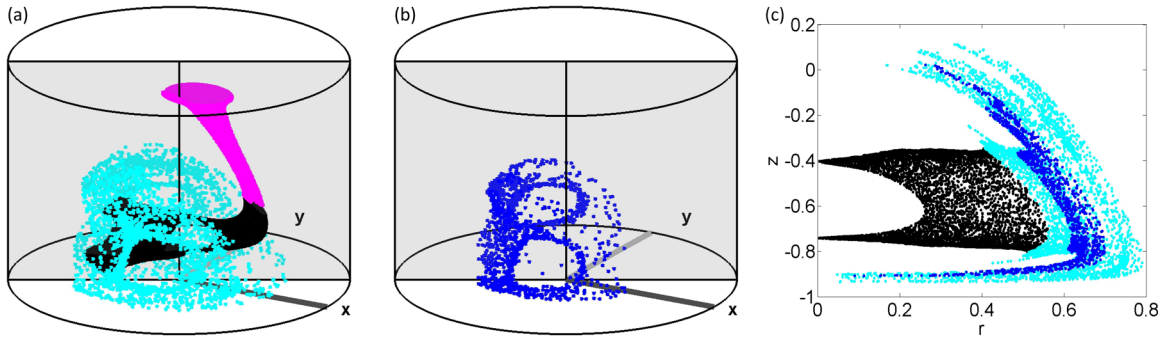

FIG. 10. Further investigation of RIM due to segmented periodic lines in Fig. 9(a). (a) Continuation of the simulated stroboscopic map of a single tracer in Fig. 9(a) (black) at parabolic points I (cyan/light gray) and IV (magenta/medium gray) forward and backward in time, respectively. (b) Experimental chaotic shell at point I. (c) Coincidence of the experimental (blue/dark gray) and simulated (cyan/light gray) chaotic shell.

Parabolic point IV sits on an entirely elliptic segment of the periodic line, implying, similar to the situation in Fig. 2(b), virtual segmentation upon perturbation. However, in contrast with a global manifestation of RIM according to Fig. 2(b), here the tube continues past the parabolic point as demonstrated in Fig. 9(a). This suggests essentially the same highly-localized manifestation of RIM as observed before for the inner tubes corresponding with the behavior in Fig. 2(b) (not shown): tracers switching tube segments via a thin hyperbolic layer. The rz projection of the stroboscopic map in Fig. 11 substantiates this by exposing a distinct gap between the tube segments (distinguished by black and magenta) on either side of parabolic point IV (green marker).

Parabolic points I and II in Fig. 9 are intersections of the segmented period-1 line in the symmetry plane (shaded) with the shown pair of period-2 lines and thus correspond with case $\alpha_p = -2$ in Fig. 7(d). The resulting period-2 resonance (Sec. V A) induces oscillatory dynamics at points I and II and this is particularly clear in the simulated stroboscopic map in Fig. 12(a). The shown tracer, namely, enters a pair of period-2 tubes, forming in the chaotic zone at point I around the unperturbed period-2 line, and thus describes a bifurcating tube. Formation of the period-2 tubes and discriminating whether tracers enter these entities (Fig. 12) or the chaotic zone (Fig. 9) is beyond the canonical map following Sec. IV B. This is an essentially nonlinear phenomenon that involves perturbation-induced interaction of chaotic trajectories around the period-1 hyperbolic segment with elliptic islands of the nearby period-2 elliptic lines emanating from said line intersections. The assumption of intrasurface Hamiltonian dynamics sufficiently far away from the integrable state implies that such islands—and the corresponding tube bifurcations—are in general highly localized (Secs. II B and IV B) and the system generically exhibits RIM following Fig. 10(a). However, the emergence of sizable bifurcating tubes as shown in Fig. 12(a) means that here islands within the intrasurface chaotic sea remain significant and the above assumption locally breaks down. The experimental stroboscopic map in Fig. 12(b) closely agrees with its computational counterpart and thus validates the tube bifurcation associated with RIM. Moreover, emergence of tube-and-shell structures due to global segmentation at point I as shown in Fig. 10(a) (black/cyan) that envelop the bifurcating tubes in Fig. 12 implies that the latter, notwithstanding their substantial size, indeed are localized nonlinear phenomena within an instance of RIM.

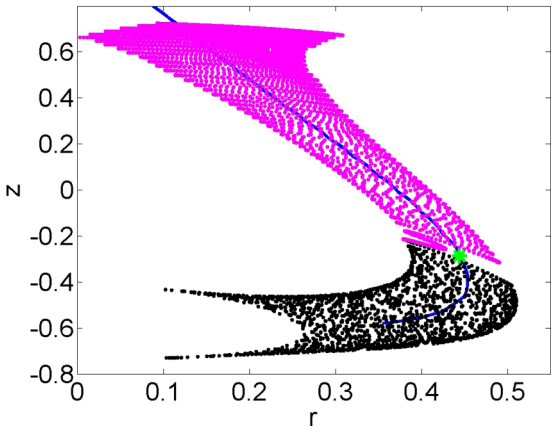

FIG. 11. Highly localized manifestation of RIM at point IV in Fig. 9(a) due to virtual segmentation upon perturbation: switching between tube segments (black and magenta/medium gray) via the hyperbolic layer at point IV (green/light gray marker).

Essentially similar manifestations of RIM due to line segmentation occur for all configurations of the 3D cylinder flow considered to date [12–14] as well as in the above-mentioned cases in the magnetic-bead-driven microflow in [15] without isolated periodic points. Hence expansion of existing theory relying on the emergence of such points (Sec. IV C) by the RIM scenarios according to Secs. V B–V D indeed yields a comprehensive theory.

VI. INVARIANT SURFACES DUE TO RIM

RIM both by periodic points and line segmentation yields invariant surfaces (cyan in Fig. 7) and thus indeed accomplishes actual tube-shell merger. Invariant surfaces associated with periodic points are parametrized by (22) for $z_* = 0$ as explained before (Sec. IV C); their formation via line segmentation is investigated below.

Consider RIM due to global segmentation of a periodic line with discriminant (26) for $\alpha_p = 2$ [Fig. 7(c)]. The corresponding invariant surface $\mathcal{S}(G)$ (cyan) consists in the elliptic

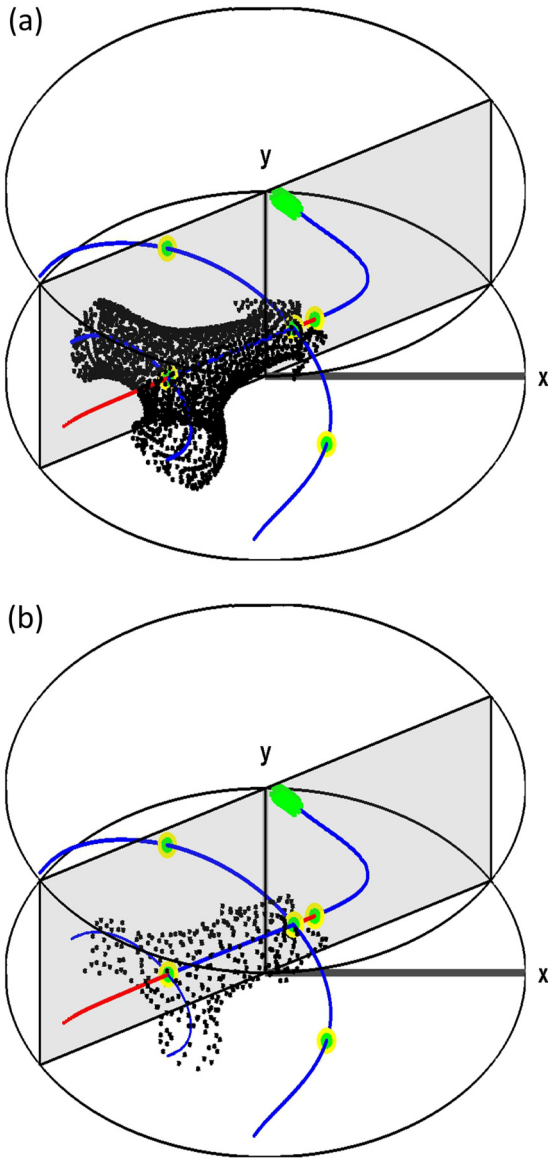

FIG. 12. Tube bifurcation by period-2 resonance ($\alpha_p = -2$) at the parabolic point (green star) between elliptic (blue/dark gray) and hyperbolic (red/light gray) segments of the period-1 line in the symmetry plane (shaded) demonstrated by the stroboscopic map of a single tracer. (a) Simulated map. (b) Experimental map.

region ($\alpha < 2$) of tubes parametrized by G following (22) and terminating in resonance sheet $z = \widetilde{z}\ (= 0)$ at circles

$$\mathcal{C}(G) : x_0^2 + y_0^2 = r_0^2 = G/(\widetilde{z} - z_*). \tag{29}$$

The extension of each invariant surface $\mathcal{S}(G)$ into the hyperbolic region ($\alpha > 2$) is composed of the union of forward mappings $\boldsymbol{M}^n(\mathcal{D})$, with $\boldsymbol{M}$ according to (7) and $n \geqslant 1$, of the tube end $\mathcal{D}$ bounded by circle $\mathcal{C}$ following (29) and its backward mapping $\boldsymbol{M}^{-1}(\mathcal{C})$. Hence the hyperbolic portion of each invariant surface smoothly "grows" out of its tube end $\mathcal{D}$ as demonstrated in Fig. 13(a) for the invariant surface (cyan) of the tracer (black orbit) in Fig. 7(c) emerging from circle $\mathcal{C}$ (magenta) centered on the parabolic point $\widetilde{z} = 0$ (black star).

The forward mappings of circle $\mathcal{C}(G)$ [cyan curves in Fig. 13(a)] bound the evolving tube ends $\mathcal{D}$ that describe the

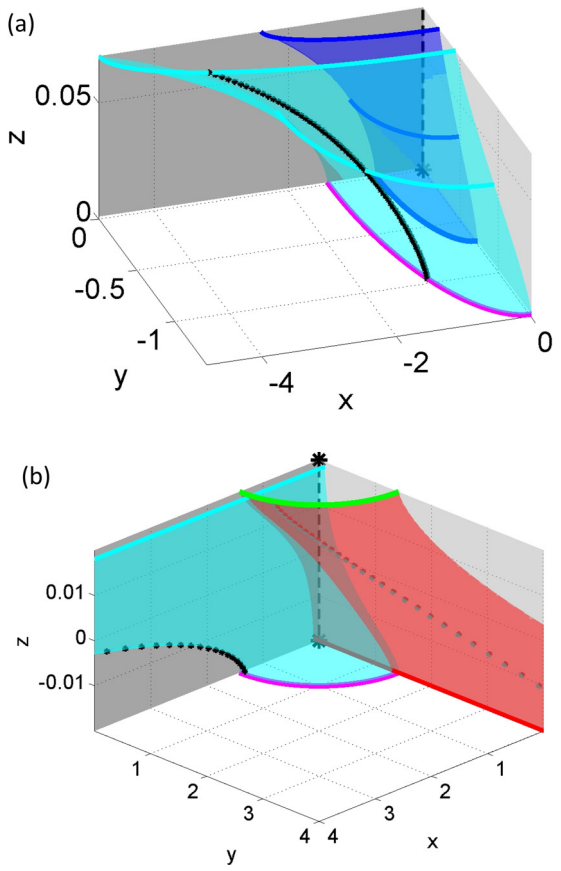

FIG. 13. Hyperbolic portions of invariant surfaces for RIM due to segmentation of the periodic line (dashed) at parabolic points (stars). (a) Invariant surface for global segmentation (cyan/light gray) for a tracer (black) expelled into a chaotic shell and neighboring surface (blue/dark gray). (b) Invariant surfaces for local segmentation (cyan/light gray and red/dark gray) for tracers (black/gray) dots expelled into/entrained from the shell. Magenta (dark gray)/green (light gray), circles connecting elliptic/hyperbolic surface portions.

invariant surface $\mathcal{S}(G)$ and are given by

$$(x_n/A^n\widetilde{\lambda}_n)^2 + (x_n\widetilde{\lambda}_n/B^n)^2 = r_0^2, \tag{30}$$

with $\widetilde{\lambda}_n = \Pi_{i=0}^{n-1}\lambda(z_i) > 1$, describing ellipses of radius

$$r_{\text{maj}} = A^n\widetilde{\lambda}_n r_0 > r_0, \quad r_{\text{min}} = B^n r_0/\widetilde{\lambda}_n < r_0, \tag{31}$$

along the major and minor axes, respectively. Thus the invariant surfaces (i) constitute (along the entire line) a continuous family of smooth surfaces $\mathcal{S}(G)$ parametrized by G that are (ii) topologically tubes and (iii) self-similar in r. Hence positions on $\mathcal{S}(G_1)$ (cyan) and $\mathcal{S}(G_2)$ (blue) in Fig. 13(a) for any $z_2 = z_1$ relate via $x_2/x_1 = y_2/y_1 = r_2/r_1$.

The exponential growth or diminution of radii $r_{\text{min,maj}}$ following (31) with progressing mapping n signifies rapid contraction and stretching of the elliptic cross section of shown invariant surfaces with increasing z in Fig. 13(a) along the minor and major axes, respectively, and reflects the impact of the stable (dark gray) and unstable (light gray) manifolds on the dynamics. This results in an extreme x-wise divergence of the invariant surfaces upon entering the hyperbolic region as predicted by (20); contrast to this end the

relative thickness $\Delta z = (z_{\max} - z_{\min})/r_0 \approx 0.05$ and aspect ratio $(x_{\max} - x_{\min})/\Delta z \approx 70$ of shown hyperbolic portions with the only minute excursion $\alpha - 2 \leqslant 7 \times 10^{-3}$ into the hyperbolic regime. Hence entering the hyperbolic region immediately triggers a sudden deflection of tracer paths into a thin chaotic shell as demonstrated in Fig. 7(c).

The above concerns expulsion of tracers from tubes into the chaotic shell via the unstable manifold for $\alpha_p = 2$ as demonstrated in Fig. 7(c) yet this readily extends to case $\alpha_p = -2$ in Fig. 7(d). Moreover, entrainment of tracers from the chaotic shell into tubes may occur [12–15,20]. The canonical map captures this by backward mapping $\boldsymbol{x}_n = \boldsymbol{M}^{-n}(\boldsymbol{x}_0)$, yielding a path that enters the tube along the stable manifold (manifolds switch stability upon time reversal). RIM at points (I,III) and II in Fig. 9(a), e.g., corresponds with expulsion and entrainment for $\alpha_p = -2$, respectively.

The invariant surfaces for local segmentation as demonstrated in Figs. 7(a) and 7(b) are in essence similar to the above global counterparts. Surfaces with an elliptical cross section following (30) emerge from the bounding circles $\mathcal{C}(G)$ following (29) of the lower tube family in resonance sheet $z = \widetilde{z} < 0$; Fig. 13(b) gives the invariant surface (cyan) and corresponding circle (magenta) for the tracer expelled from the lower tube (black orbit) in Fig. 7(a) for $\alpha_p = 2$. The principal difference with global segmentation is that simultaneously entrainment of tracers from the chaotic sea into the upper tube family across the hyperbolic region bounded by resonance sheet $z = \widetilde{z} > 0$ occurs. The corresponding invariant surfaces are demarcated by backward mappings of the tube end attached to the upper bounding circles $\mathcal{C}(G)$. Figure 13(b) gives this circle (green) and resulting surface (red) for a tracer passing through $\boldsymbol{x}_n' = -\boldsymbol{x}_0$, with $\boldsymbol{x}_0$ the initial position of the tracer expelled via the cyan surface, and following the gray orbit during entrainment.

Thus two families of invariant surfaces emerge for RIM due to (virtual) local segmentation [Fig. 13(b)]: surfaces $\mathcal{S}_R(G)$ associated with tracer expulsion into the chaotic shell from one tube family (cyan) via the unstable (dark gray) manifold and surfaces $\mathcal{S}_A(G)$ associated with tracer entrainment from this shell into the companion tube family (red) via the stable (light gray) manifold. Thus former and latter tube families behave as repellers ("R") and attractors ("A") for the tracer dynamics. Both processes involve, as before, sudden deflection of the tracer paths due to extreme divergence of surfaces $\mathcal{S}_{R,A}$ in the hyperbolic region [relative thickness $\Delta z \approx 0.03$ and aspect ratio $(x_{\max} - x_{\min})/\Delta z \approx 1000$ for $\alpha - 2 \leqslant 10^{-2}$].

Simultaneous expulsion into and entrainment from the chaotic shell causes certain tracers to cross over from the tubes in $\mathcal{S}_R$ to those in $\mathcal{S}_A$. This is reminiscent of "scattering" following [7] yet here occurs, instead of via defects in tubes, through a finite-thickness hyperbolic layer separating two tube families. The corresponding paths coincide with the intersections

$$\mathcal{L}(G_1, G_2) = \mathcal{S}_R(G_1) \cap \mathcal{S}_A(G_2), \tag{32}$$

and the subset of tracers crossing over is determined by the radial extent of the tubes. The parameters are, namely, bounded as $0 \leqslant G_{1,2} \leqslant G_{\max}$, with $G_{\max} = r_{\max}^2(z_* - z_{\mathrm{ref}})$ and $r_{\max}$ the maximum tube radius at an arbitrary reference plane $z = z_{\mathrm{ref}}$. This restricts tracers crossing over to but a small subset; the vast majority is expelled into the chaotic shell. Consider for illustration the lower/upper tube families demarcated by the magenta/green circles in Fig. 13(b). The intersection curve of $\mathcal{S}_A$ (red) and $\mathcal{S}_R$ (cyan) describes one "cross-over" path following (32) in the shown quadrant; a companion path is defined in the same way in each of the other quadrants. This reveals that only tracers exiting the lower tube family in the narrow strip bounded by the intersection of $\mathcal{S}_A$ with the lower interface of the hyperbolic layer (red curve within magenta circle) and the y axis enter the upper tube family; all other tracers exiting the lower tube family are expelled into the chaotic shell.

The emergence and structure of invariant surfaces for *actual* local segmentation readily generalize to *virtual* local segmentation. Essentially similar hyperbolic portions of invariant surfaces as in Fig. 13(b), e.g., emanate for the case shown in Fig. 8(a) from circular tube ends (green/magenta) in z-wise planes attached to the end points $z = \pm\widetilde{z}_*$ (stars) of the line segment $-\widetilde{z}_* \leqslant z \leqslant \widetilde{z}_*$ (dashed) on the periodic line that meets condition (27).

It must be stressed that strict differentiation between global and local segmentation may be difficult (if not impossible) in realistic flows. Revisit to this end the typical manifestations of RIM due to line segmentation discussed in Sec. V E and shown in Fig. 9. The extent of the segments demarcated by parabolic points II and III implies *global* segmentation yet the interaction between invariant surfaces is reminiscent of *local* segmentation. Thus the dynamics in realistic flows may exhibit features of both RIM scenarios. However, this is inconsequential for the validity and universality of the phenomena described above.

VII. CONCLUSIONS

The scope of the present paper is the response of Lagrangian flow topologies of 3D time-periodic flows consisting of spheroidal invariant surfaces to perturbation. Such invariant surfaces generically accommodate nonintegrable Hamiltonian dynamics and, in consequence, intrasurface topologies composed of islands and chaotic seas. Computational studies predict a response to arbitrary perturbation that is dramatically different from the classical case of toroidal invariant surfaces: said islands and chaotic seas evolve into tubes and shells, respectively, that merge into "tube-and-shell" structures consisting of two shells connected via (a) tube(s) by a mechanism termed "resonance–induced merger". This paper provides conclusive experimental proof of RIM by direct measurements of long-term Lagrangian motion of passive tracers by 3D particle-tracking velocimetry. Moreover, these 3DPTV studies demonstrate that the underlying unperturbed state is a singular limit that exists only for ideal conditions and cannot be achieved in a physical experiment. Hence the perturbed state of tube-and-shell structures constitutes the physical topology in realistic 3D unsteady flows with spheroidal invariant surfaces accommodating dynamics sufficiently away from the integrable state.

A comprehensive theory (supported by 3DPTV experiments) reveals that RIM ensues from perturbed periodic lines (i.e., curves consisting of material points that systematically

return to their initial position) via three possible scenarios: truncation of tubes by (i) manifolds of isolated periodic points emerging near elliptic lines or by either (ii) local or (iii) global segmentation of periodic lines into elliptic and hyperbolic parts. The RIM scenario for local segmentation includes a perturbation-induced change from elliptic to hyperbolic dynamics near degenerate points on entirely elliptic lines (denoted "virtual local segmentation"). This theory furthermore demonstrates that RIM indeed accomplishes tube-shell merger by exposing the existence of invariant surfaces that smoothly extend from the tubes into the chaotic shells. These phenomena set the response to perturbation—and physical topology—of flows with spheroidal invariant surfaces fundamentally apart from flows with toroidal invariant surfaces.

The comprehensive theory is entirely of a kinematic nature and employs canonical representations of the Lagrangian dynamics that rely solely on continuity and solenoidality of the underlying velocity field. This renders the theory and its findings universal and generically applicable for (arbitrary perturbation of) basically any incompressible flow—in fact any smooth solenoidal vector field—accommodating spheroidal invariant surfaces. The consistent emergence of RIM in the unsteady cylinder flow adopted in the current paper for a variety of perturbations as well as occurrence of essentially similar instances of RIM in other flows support this assertion.

Nontoroidal invariant surfaces of greater topological complexity as well as quasi-2D representations of Lagrangian transport in geophysical flows accommodate similar Hamiltonian dynamics as the spheroidal invariant surfaces. This strongly suggests that the response to perturbation (including formation of tube-and-shell structures) likely generalizes to a broader class of systems involving restriction of Lagrangian motion to (subregions of) nontoroidal invariant surfaces. Efforts to address this matter are underway.

ACKNOWLEDGMENTS

The authors sincerely acknowledge A. P. C. Holten and F. M. R. van Uittert for their technical support and G. Metcalfe (Swinburne University of Technology, Melbourne, Australia) for scientific discussions on the phenomena reported here. P.S.C. gratefully acknowledges financial support by the Consejo Nacional de Ciencia y Tecnología (CONACYT) Mexico.

APPENDIX A: UNPERTURBED CANONICAL MAP

The canonical map (7) leans on the spectral decomposition of the linearized map $\boldsymbol{\mathcal{F}}_0$ following (6), i.e.,

$$\boldsymbol{\mathcal{F}}_0 = \boldsymbol{V}\boldsymbol{\Lambda}\boldsymbol{V}^{-1}, \tag{A1}$$

with $\boldsymbol{V} = [\boldsymbol{v}_1\ \boldsymbol{v}_2\ \boldsymbol{v}_3]$ and $\boldsymbol{\Lambda} = \mathrm{diag}(\lambda_1, \lambda_2, \lambda_3)$ the eigenvector and eigenvalue matrices, respectively. The eigenvalue spectrum is governed by the characteristic equation

$$|\boldsymbol{\mathcal{F}}_0 - \lambda \boldsymbol{I}| = \lambda^3 - J_1\lambda^2 + J_2\lambda - J_3 = 0, \tag{A2}$$

which is determined by the matrix invariants

$$J_1 = \mathrm{tr}(\boldsymbol{\mathcal{F}}_0),\ J_2 = \tfrac{1}{2}\left[\mathrm{tr}^2(\boldsymbol{\mathcal{F}}_0) - \mathrm{tr}\left(\boldsymbol{\mathcal{F}}_0^2\right)\right],\ J_3 = \det(\boldsymbol{\mathcal{F}}_0),$$

where $J_3 = 1$ due to $\boldsymbol{\nabla}\cdot\boldsymbol{u} = 0$. For periodic lines $J_1 = J_2$, implying one unit eigenvalue, say

$$\lambda_3 = 1, \tag{A3}$$

and yielding two nondegenerate cases for (λ_1, λ_2), i.e.,

$$\lambda_1 = \lambda_2^{-1} = \lambda = \alpha/2 + \sqrt{(\alpha/2)^2 - 1} \tag{A4}$$

for $|\alpha| > 2$ and

$$\lambda_1 = \lambda_2^* = \alpha/2 + \mathrm{i}\sqrt{1 - (\alpha/2)^2} \tag{A5}$$

for $|\alpha| < 2$, with discriminant α given by

$$\alpha = J_1 - 1, \tag{A6}$$

and $i = \sqrt{-1}$ (superscript "$*$" indicates complex conjugate) [23]. This gives

$$\boldsymbol{\zeta}_{n+1} = \boldsymbol{\Lambda}\boldsymbol{\zeta}_n, \quad \boldsymbol{\zeta} = \boldsymbol{V}^{-1}\boldsymbol{\xi}', \tag{A7}$$

as representation of the linearized map (6) in the eigenspace $\boldsymbol{\zeta}$ spanned by eigenvectors $\boldsymbol{v}_k$. Reformulating the complex notation in the $\zeta_{1,2}$ direction for case $|\alpha| < 2$ due to complex $\lambda_1 = \lambda_2^*$ (and corresponding $\boldsymbol{v}_1 = \boldsymbol{v}_2^*$) following (A5) into standard Cartesian form (x, y) admits translation of (A7) for any α into a single canonical map (7) in eigenspace $\boldsymbol{x} = (x, y, z)$ via (trivial) transformation

$$\boldsymbol{x} = \boldsymbol{\zeta}, \quad \boldsymbol{F}_0 = \boldsymbol{\Lambda} = \begin{bmatrix} \lambda & 0 & 0 \\ 0 & \lambda^{-1} & 0 \\ 0 & 0 & 1 \end{bmatrix}, \tag{A8}$$

for $|\alpha| > 2$ and transformation

$$\boldsymbol{x} = \left(\frac{\zeta_1 + \zeta_2}{2}, \frac{\zeta_1 - \zeta_2}{2\mathrm{i}}, \zeta_3\right), \quad \boldsymbol{F}_0 = \begin{bmatrix} c & -s & 0 \\ s & c & 0 \\ 0 & 0 & 1 \end{bmatrix}, \tag{A9}$$

for $|\alpha| < 2$, with

$$c = \cos\mu = \alpha/2, \quad s = \sin\mu = \sqrt{1 - c^2} \tag{A10}$$

the real and imaginary parts, respectively, of eigenvalue λ_1 of magnitude $|\lambda_1| = 1$ given in (A5). The periodic line in canonical space $\boldsymbol{x}$ thus defined coincides with the z axis and planes $z = \mathrm{const}$ represent the invariant surfaces.

APPENDIX B: PERTURBED CANONICAL MAP

The above unperturbed canonical map is nonlinear via the dependence of discriminant (11) on the normal coordinate z yet with a special structure in that the dynamics are linear in the planar coordinates (x, y) within an invariant surface $z = \mathrm{const}$. Perturbations are assumed sufficiently small so that (in accordance with conventional perturbation theory) the perturbed system retains the piecewise linear structure of the unperturbed system. Arbitrary perturbation under this premise extends canonical map (7) to

$$\boldsymbol{x}_{n+1} = \boldsymbol{F}\boldsymbol{x}_n + \boldsymbol{d}, \tag{B1}$$

with corresponding perturbed linear operator

$$\boldsymbol{F} = \boldsymbol{F}'\boldsymbol{F}_0, \quad \boldsymbol{F}' = \begin{bmatrix} A & a_2 & a_3 \\ b_1 & B & b_3 \\ c_1 & c_2 & C \end{bmatrix}, \tag{B2}$$

where $(A, B, C) = (1 + a_1, 1 + b_2, 1 + c_3)$, and background drift $\boldsymbol{d} = (d_1, d_2, d_3)$. Parameters $a_i, b_i, c_i \sim O(\epsilon_1)$ and $d_i \sim O(\epsilon_2)$, with $\epsilon_{1,2} \ll 1$, control the perturbation.

The perturbed map admits simplification without loss of generality as follows. Characteristic equation (A2) for $\boldsymbol{F}_0$ following (A8) subject to perturbation (B2) becomes

$$\begin{aligned}|\boldsymbol{F} - \lambda'\boldsymbol{I}| &= (C - \lambda')[(A\lambda - \lambda')(B/\lambda - \lambda') - a_2 b_1] \\ &\quad - (c_2/\lambda)[(A\lambda - \lambda')b_3 - a_3 b_1 \lambda] \\ &\quad + c_1\lambda[a_2 b_3/\lambda - a_3(B/\lambda - \lambda')] \\ &= (C - \lambda')(A\lambda - \lambda')(B/\lambda - \lambda') + O\big(\epsilon_1^2\big) \\ &= 0, \end{aligned} \tag{B3}$$

where the trailing term in the bottom line collects all contributions involving multiplication factors consisting of (triple) products of a_i, b_i, c_i. Omitting the latter yields

$$\lambda_1' = A\lambda, \quad \lambda_2' = B/\lambda, \quad \lambda_3' = C, \tag{B4}$$

as leading-order approximation of the eigenvalue spectrum of the perturbed operator $\boldsymbol{F}$ in regime $|\alpha| > 2$. Similarly, characteristic equation (A2) for $\boldsymbol{F}_0$ following (A9) subject to perturbation (B2) becomes

$$\begin{aligned}|\boldsymbol{F} - \lambda'\boldsymbol{I}| &= (C - \lambda')\{\lambda'^2 - \gamma\lambda' + AB\} + O(\epsilon_1^2) \\ &= 0, \end{aligned} \tag{B5}$$

with $\gamma = (A + B)c + (a_2 - b_1)s$ and (c, s) according to (A10), where again omitting the trailing term yields

$$\lambda_1' = \lambda_2'^{*} = \sqrt{AB}(c' + \mathrm{i}\sqrt{1 - c'^2}), \quad \lambda_3' = C, \tag{B6}$$

with

$$c' = \frac{\gamma}{2\sqrt{AB}} = \cos\mu' \approx \frac{(A + B)c}{2\sqrt{AB}} \tag{B7}$$

as leading-order approximation of the eigenvalue spectrum of the perturbed operator $\boldsymbol{F}$ in regime $|\alpha| < 2$. The above leading-order approximations of the characteristic equations and corresponding eigenvalue spectra of the linearized perturbed system constitute, essentially similar to the study in [6], the backbone of the present investigation of the perturbed dynamics and admit simplification of canonical map (B1) as described below.

Dependence of the leading-order approximations (B4) and (B6) of the perturbed eigenvalues $\boldsymbol{\lambda}' = (\lambda_1', \lambda_2', \lambda_3')$ for $|\alpha| > 2$ and $|\alpha| < 2$, respectively, solely on coefficients (A, B, C) implies that only the diagonal elements of the perturbation matrix $\boldsymbol{F}'$ in (B2) are relevant and thus effectively simplifies to $\boldsymbol{F}' = \mathrm{diag(A, B, C)}$. This yields

$$\boldsymbol{F} = \begin{bmatrix} A\lambda & 0 & 0 \\ 0 & B/\lambda & 0 \\ 0 & 0 & C \end{bmatrix}, \quad \boldsymbol{F} = \begin{bmatrix} Ac & -As & 0 \\ Bs & Bc & 0 \\ 0 & 0 & C \end{bmatrix}, \tag{B8}$$

as perturbed linear operator (B2) for $|\alpha| > 2$ and $|\alpha| < 2$, respectively. The solenoidality condition $\det(\boldsymbol{F}) = \det(\boldsymbol{F}')\det(\boldsymbol{F}_0) = 1$ leads to $\det(\boldsymbol{F}') = 1 = ABC + O(\epsilon_1^2)$ and, by virtue of $\epsilon_{1,2} \ll 1$, $ABC = 1$ for the leading-order approximation (B8). Restriction of (without loss of generality) the isolated periodic point

$$\boldsymbol{x}_* = (\boldsymbol{I} - \boldsymbol{F})^{-1}\boldsymbol{d}, \tag{B9}$$

of mapping (B1) to the z axis, i.e., $\boldsymbol{x}_* = (0, 0, z_*)$, gives

$$\boldsymbol{d} = (0, 0, -c_3 z_*) \equiv (0, 0, \epsilon_2), \tag{B10}$$

as corresponding (purely z-wise) background drift.

Linear operator $\boldsymbol{F}$ in (B8) for case $|\alpha| > 2$ adopts the general structure of its unperturbed counterpart $\boldsymbol{F}_0$ following (A8) and thus qualitative retains the (hyperbolic) nature of the unperturbed dynamics. This qualitative retention of the unperturbed dynamics, though less evident, also holds for case $|\alpha| < 2$. The corresponding operator $\boldsymbol{F}$ in (B8), namely, satisfies characteristic equation (B5), implying an embedded elliptic structure similar to (A9) yet based on eigenvalues (B6) instead of (A5), i.e.,

$$\widetilde{\boldsymbol{F}} = \begin{bmatrix} \dfrac{c'}{\sqrt{C}} & -\dfrac{s'}{\sqrt{C}} & 0 \\ \dfrac{s'}{\sqrt{C}} & \dfrac{c'}{\sqrt{C}} & 0 \\ 0 & 0 & C \end{bmatrix}, \tag{B11}$$

using $s' = \sqrt{1 - c'^2}$ and $C = 1/AB$. Similarity transform

$$\boldsymbol{F} = M\widetilde{\boldsymbol{F}}M^{-1}, \quad \boldsymbol{M} = \begin{bmatrix} 1 & 0 & 0 \\ m_1 & m_2 & 0 \\ 0 & 0 & 1 \end{bmatrix} \tag{B12}$$

relates operators $\boldsymbol{F}$ and $\widetilde{\boldsymbol{F}}$, with

$$m_1 = \frac{\sqrt{B(c'^2 - c^2)}}{\sqrt{A(1 - c^2)}}, \quad m_2 = \sqrt{\frac{B}{A} - m_1^2}, \tag{B13}$$

and admits expression of (B1) as

$$\widetilde{\boldsymbol{x}}_{n+1} = \widetilde{\boldsymbol{F}}\widetilde{\boldsymbol{x}}_n + \widetilde{\boldsymbol{d}}, \tag{B14}$$

where $\boldsymbol{x} = M\widetilde{\boldsymbol{x}}$ and $\boldsymbol{d} = M\widetilde{\boldsymbol{d}} = \boldsymbol{d}$. Conditions $|c| < 1$ and $c' \approx c$ due to $|\alpha| < 2$ and $A, B \sim O(1)$, respectively, imply a nonzero and bounded determinant

$$\det(M) = m_2 = \frac{\sqrt{B(1 - c'^2)}}{\sqrt{A(1 - c^2)}}, \tag{B15}$$

and thus render similarity transform (B12) nonsingular. Hence representations (B1) and (B14) of the perturbed canonical map are entirely equivalent and interchangeable; the present paper adopts (B14) (upon dropping tildes for brevity) due to the structure of the associated $\widetilde{\boldsymbol{F}}$ following (B11) being identical to $\boldsymbol{F}_0$ in (A9).

APPENDIX C: PLANAR VERSUS NORMAL DISPLACEMENT NEAR PERTURBED PERIODIC LINES

1. Hyperbolic lines

Consider regime $\alpha > \alpha_p$ bounded by parabolic limit $\alpha_p = 2$, yielding $\lambda > \lambda_p$, with $\lambda_p = 1$, and thus designating the x axis as the unstable manifold in the unperturbed planar motion (12). This results in x-wise exponential divergence following $x_{n+1} = A\lambda x_n$ in the perturbed state (15) and $z_{n+1} = Cz_n + \epsilon_2$ as corresponding normal (i.e., z-wise) motion. Thus the ratio planar-to-normal motion becomes

$$\frac{x_{n+1} - x_n}{z_{n+1} - z_n} = \frac{(A\lambda - 1)x_n}{(C - 1)z_n + \epsilon_2}, \tag{C1}$$

which to good approximation simplifies to

$$\frac{x_{n+1}-x_n}{z_{n+1}-z_n} \approx \gamma_h x_n, \quad \gamma_h = \frac{(\lambda-1)}{\epsilon_2}, \tag{C2}$$

in the absence of isolated points (implying $|C-1| = \epsilon_2/|z_*| \ll \epsilon_2$ and, in consequence, $z_{n+1}-z_n \approx \epsilon_2$ due to $|z_*| \gg 1$) and using $A \approx 1$. Minute excursions $\alpha - \alpha_p \gtrsim O(10^{-2})$ into the hyperbolic regime already give rise to substantial departures $\lambda - 1 = \lambda - \lambda_p \gtrsim O(0.1)$ of coefficient λ from its parabolic limit $\lambda_p = 1$. This, in conjunction with condition $\epsilon_2 \ll 1$, yields

$$\gamma_h \gg 1, \tag{C3}$$

and through (C2) implies a rapid x-wise divergence of Lagrangian trajectories from the periodic line before any appreciable z-wise drift can develop. Hence tracers (at least in the proximity of the original periodic line) remain close to the associated unperturbed invariant surface as demonstrated in Figs. 7(a) and 7(c) by the sudden deflection of the tracer path upon reaching the hyperbolic segment of the periodic line. Excursion into hyperbolic regime $\alpha < \alpha_p$, with $\alpha_p = -2$, similarly results in rapid y-wise divergence following Figs. 7(b) and 7(d).

2. Elliptic lines

Radial motion is in the elliptic regime $|\alpha| < 2$ of the perturbed state (15) (using identity $c'^2 + s'^2 = 1$) described by $r_{n+1} = \sqrt{x_{n+1}^2 + y_{n+1}^2} = r_n/\sqrt{C}$. Combination with relation $z_{n+1} = Cz_n + \epsilon_2$ as before gives

$$\frac{r_{n+1}-r_n}{z_{n+1}-z_n} = \frac{(1/\sqrt{C}-1)r_n}{(C-1)z_n+\epsilon_2}, \tag{C4}$$

for the ratio planar-to-normal motion. This, similar to (C1), to good approximation simplifies to

$$\frac{r_{n+1}-r_n}{z_{n+1}-z_n} \approx \gamma_e r_n, \quad \gamma_e = \frac{1-\sqrt{C}}{\sqrt{C}\epsilon_2}, \tag{C5}$$

in the absence of isolated points. Condition $|C-1| \ll \epsilon_2$ due to absence of these points (Appendix C1) admits linearization of (C5) around $C = 1$ and thus yields

$$|\gamma_e| = \frac{|C-1|}{2\epsilon_2} \ll 1, \tag{C6}$$

implying a reversed situation compared to the above hyperbolic case in that planar motion is negligible. This causes prolonged entrapment in the proximity of the original periodic line and, in consequence, an appreciable z-wise drift away from the unperturbed invariant surface. This is demonstrated in Figs. 7(a)–7(d) by the spiralling tracer path centered on the elliptic segment of the periodic line.

APPENDIX D: VIRTUAL LOCAL SEGMENTATION OF ELLIPTIC LINES NEAR PARABOLIC POINTS

A fundamental departure from the generic response to perturbation (Appendix B) relevant in the context of RIM occurs near parabolic points ($\alpha_p = \pm 2$) on otherwise entirely elliptic lines ($|\alpha| < 2$). The perturbed dynamics near such lines is governed by characteristic equation (B5) and its nature is determined by the eigenvalue pair $\lambda'_{1,2}$ corresponding with the characteristic equation

$$\lambda'^2 - \gamma\lambda' + AB = 0, \quad \gamma = (A+B)c, \tag{D1}$$

embedded in (B5). Standard algebra readily yields two solutions depending on discriminant

$$D = \gamma^2 - 4AB = (A+B)^2c^2 - 4AB, \tag{D2}$$

namely, $\lambda'_1 = \lambda'^*_2$ following (B6) for $D < 0$ and

$$\lambda'_{1,2} = \sqrt{AB}(c' \pm \sqrt{c'^2-1}), \quad c' = \frac{(A+B)c}{2\sqrt{AB}}, \tag{D3}$$

for $D > 0$. Generically $D < 0$ and thus the former solution holds, meaning that the perturbed dynamics indeed retains the qualitative (elliptic) nature of the unperturbed dynamics as per Appendix B. In the direct proximity of parabolic points, on the other hand, any perturbation gives $D > 0$ and results in a qualitative change in dynamics from elliptic to hyperbolic behavior. Discriminant (D2) via $c = \alpha/2 = \pm 1$, namely, becomes $D = (A+B)^2 - 4AB = (a_1 - b_2)^2$ at parabolic points $\alpha = \pm 2$, implying $D > 0$ for any nonzero $a_1 \neq b_2$.

Expressing eigenvalue pair $\lambda'_{1,2}$ in (B4) for perturbed hyperbolic lines in the alternative form

$$\lambda'_{1,2} = \sqrt{AB}(\widetilde{c} \pm \sqrt{\widetilde{c}^2-1}), \quad \widetilde{c} = \frac{A\lambda + B/\lambda}{2\sqrt{AB}} \tag{D4}$$

reveals that eigenvalue pair $\lambda'_{1,2}$ following (D3) adopts the same form as its counterpart in (B4) upon substitution of $\widetilde{c} = c'$. This demonstrates that the perturbed behavior near parabolic points on an elliptic line (i.e., for case $D > 0$) and a hyperbolic line is indeed essentially equivalent. This implies a "virtual local segmentation" of the elliptic line in that the corresponding perturbed dynamics, though predominantly retaining the elliptic nature, near parabolic points is the same as for a hyperbolic line.

Segments of elliptic lines at parabolic points undergoing the above qualitative change in dynamics are demarcated by a corresponding discriminant α in the range

$$\alpha_{\min} \leqslant |\alpha| \leqslant 2, \quad \alpha_{\min} = \frac{4\sqrt{AB}}{A+B} \leqslant 2, \tag{D5}$$

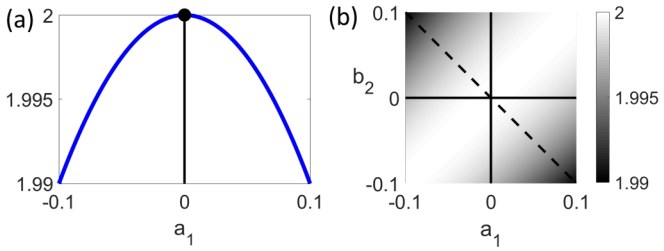

FIG. 14. Lower bound $\alpha_{\min}$ of the range for discriminant α according to (D5) resulting in qualitative change near the elliptic line from elliptic to hyperbolic dynamics upon perturbation. (a) $\alpha_{\min}$ for $a_1 = -b_2$. (b) $\alpha_{\min}$ for generic (a_1, b_2) [the dashed line indicates the simplified case in panel (a)].

which readily follows from (D2) using $c = \alpha/2$. Figure 14(a) gives $\alpha_{\min}$ for the simplified case $a_1 = -b_2$, i.e., $\alpha_{\min} = 2\sqrt{1-a_1^2}$, exposing an only marginal widening of regime (D5) with increasing perturbation $a_1 \neq 0$ (e.g., $\alpha_{\min} \approx 1.99$ for $|a_1| \approx 0.1$). This regime remains very narrow for any $a_1, b_2 \neq 0$, as demonstrated in Fig. 14(b), and thus generically confines line segments meeting (D5) to the direct proximity of parabolic points.

[1] V. Arnol'd, *Mathematical Methods of Classical Mechanics*, Graduate Texts in Mathematics (Springer, New York, 1978).

[2] C. Q. Cheng and Y. S. Sun, Celest. Mech. **47**, 275 (1990).

[3] C. Q. Cheng and Y. S. Sun, Celest. Mech. **47**, 293 (1990).

[4] H. Aref, J. R. Blake, M. Budisic, S. S. S. Cardoso, J. H. E. Cartwright, H. J. H. Clercx, K. El Omari, U. Feudel, R. Golestanian, E. Gouillart *et al.* Rev. Mod. Phys. **89**, 025007 (2017).

[5] J. H. E. Cartwright, M. Feingold, and O. Piro, J. Fluid Mech. **316**, 259 (1996).

[6] I. Mezić, Phys. D **154**, 51 (2001).

[7] D. L. Vainchtein, A. I. Neishtadt, and I. Mezić, Chaos **16**, 43123 (2006).

[8] D. L. Vainchtein, J. Widloski, and R. O. Grigoriev, Phys. Rev. Lett. **99**, 094501 (2007).

[9] M. F. M. Speetjens, G. Metcalfe, and M. Rudman, arXiv:1904.07580 (2019).

[10] J. Pedlosky, *Geophysical Fluid Dynamics* (Springer, New York, 1992).

[11] Nonintegrable Hamiltonian dynamics and the corresponding complex intrasurface flow topologies are (at least kinematically) possible also in toroidal invariant surfaces [17]. However, such surfaces emerge in incompressible flows normally only as KAM tori described by helical trajectories. Thus nonintegrable Hamiltonian dynamics and complex intrasurface flow topologies are generically restricted to nontoroidal invariant surfaces.

[12] M. F. M. Speetjens, H. J. H. Clercx, and G. J. F. van Heijst, Phys. Fluids **18**, 83603 (2006).

[13] M. F. M. Speetjens, H. J. H. Clercx, and G. J. F. van Heijst, Chaos **16**, 43104 (2006).

[14] Z. Pouransari, M. F. M. Speetjens, and H. J. H. Clercx, J. Fluid Mech. **654**, 5 (2010).

[15] N. R. Moharana, M. F. M. Speetjens, R. R. Trieling, and H. J. H. Clercx, Phys. Fluids **25**, 093602 (2013).

[16] I. Christov, R. Lueptow, J. Ottino, and R. Sturman, SIAM J. Appl. Dyn. Sys. **13**, 901 (2014).

[17] A. Gómez and J. D. Meiss, Chaos **12**, 289 (2002).

[18] S. Wiggins, Annu. Rev. Fluid Mech. **37**, 295 (2004).

[19] H. Dijkstra, *Nonlinear Physical Oceanography: A Dynamical Systems Approach to the Large Scale Ocean Circulation and El Nino* (Springer, New York, 2005).

[20] F. Wu, M. F. M. Speetjens, D. L. Vainchtein, R. R. Trieling, and H. J. H. Clercx, Phys. Rev. E **90**, 063002 (2014).

[21] Namely, exact placement of tracers at designated positions in the experimental setup is very challenging. Hence tracers are released as accurately as possible in the laboratory experiments and the initial conditions of the simulations of the (un)perturbed systems are subsequently identified with the starting positions of tracer paths determined by 3DPTV. This*a posteriori* eliminates any positioning errors and thus admits a one-to-one comparison between simulated and experimental dynamics.

[22] J. Znaien, M. F. M. Speetjens, R. R. Trieling, and H. J. H. Clercx, Phys. Rev. E **85**, 066320 (2012).

[23] This derivation of the eigenvalues essentially follows that of [15] yet with different parametrization.